FREIE UNIVERSITÄT BERLIN

Department of Physics
Arnimallee 14, 14195 Berlin

Efficient calculation of optical spectra of materials with strong spin-orbit coupling

Seokhyun Hong

hongs95@zedat.fu-berlin.de

External Supervisor: Prof. Dr. Claudia Draxl

claudia.draxl@physik.hu-berlin.de

First Supervisor: Prof. Dr. Karsten Reuter

reuter@fhi.mpg.de

Second Supervisor: PD. Dr. Stefan Ludwig

ludwig@pdi-berlin.de

Date of submission: 8th December, 2025

Abstract

Spin-orbit coupling (SOC) is often crucial for calculating the optical properties of materials, particularly those containing heavy atoms. Incorporating SOC effects into calculations using the Bethe–Salpeter equation (BSE) framework poses significant computational challenges. This thesis proposes an efficient approach by implementing a recently developed second-variational with local orbital (SVLO) method within the BSE framework. Previously shown to be efficient for DFT ground-state calculations in systems with strong SOC, the SVLO method explicitly adds local orbitals at the second-variational step to enhance computational efficiency. In this thesis, the SVLO method was applied to the calculation of momentum and plane-wave matrix elements, essential ingredients of the BSE. Through this implementation, we demonstrate enhanced accuracy and efficiency of the SVLO–BSE method for materials with strong SOC. For γ-$CsPbI_3$, SVLO achieved convergence with approximately 200 empty states, whereas the standard method required 4000.

List of Figures

2.1 Comparison of the radial behavior of p-type orbitals for Pb 8

4.1 Optical absorption spectra of MoS_2 comparing SVLO and SV methods. (a,b) Singlet BSE; (c,d) RPA; (e,f) IP. 27

4.2 Convergence summary for MoS_2 (SVLO vs SV). (a,b) Singlet BSE vs $\langle xs \rangle$ *nempty*, $\langle screen \rangle$ *nempty*; (c,d) IP/RPA vs $\langle xs \rangle$ *nempty*. 28

4.3 Optical absorption spectra of PbI_2 comparing SVLO and SV methods. (a,b) Singlet exciton spectra showing perfect agreement between SVLO and SV. (c,d) RPA spectra exhibiting identical results. (e,f) IP spectra with matching absorption edges. 31

4.4 Comparison of SVLO singlet spectra with standard p-type and Dirac-type $p_{1/2}$ local orbitals showing the effect of improved relativistic treatment. (a) In-plane polarization. (b) Out-of-plane polarization. 32

4.5 Convergence of singlet optical spectra of PbI_2 with respect to $\langle xs \rangle$ *nempty*. (a,c) SVLO converges with 50 empty states. (b,d) SV takes 400 empty states for similar convergence. 33

4.6 Convergence of excitonic energy levels for PbI_2. (a) Singlet exciton with $\langle xs \rangle$ *nempty*. (b) Singlet exciton with $\langle screen \rangle$ *nempty*. (c,d) Convergence of IP and RPA exhibiting similar features between SVLO and SV at 1.66 eV. . . 34

4.7 Optical absorption spectra of $CsPbI_3$ comparing SVLO and SV methods. (a,b) Singlet BSE; (c,d) RPA; (e,f) IP. 36

4.8 Effect of Dirac-type $p_{1/2}$ local orbitals on $CsPbI_3$ singlet spectra. 37

4.9 Convergence of singlet BSE spectra for $CsPbI_3$. 37

4.10 Exciton energy convergence for $CsPbI_3$. 38

4.11 Optical absorption spectra of Cs_2PbI_4, comparing SVLO and SV. (a,b) Singlet BSE; (c,d) RPA; (e,f) IP. 41

4.12 Convergence of characteristic energies in Cs_2PbI_4 with SVLO and SV. 42

4.13 Convergence of singlet BSE spectra for Cs_2PbI_4. 43

4.14 Optical absorption spectra of $Cs_4AgBiBr_8$ at the singlet BSE level. (a) in-plane (b) out-of-plane. SVLO(p) and SVLO($p_{1/2}$) give essentially identical spectra over the shown range, with a slight redshift for $p_{1/2}$. 45

Contents

Abstract 3

List of Figures 5

1 Introduction 1

2 Theoretical Background 3

2.1 Density Functional Theory . . . 3
2.2 Hohenberg-Kohn theorem . . . 3
2.3 Kohn-Sham equation . . . 4
2.4 Linearized Augmented Planewave Method . . . 5
2.5 Local Orbital . . . 7
2.6 Dirac Type Local Orbital . . . 7
2.7 Relativistic Treatment . . . 9
2.7.1 Non-Perturbative Treatment . . . 9
2.7.2 Scalar-Relativistic Treatment . . . 10
2.7.3 Second Variational Treatment . . . 10
2.7.4 Second Variation with Local Orbital Method . . . 11
2.8 Many-Body Perturbation Theory . . . 12
2.8.1 Screened Coulomb interaction in MBPT . . . 12
2.8.2 Dielectric Function . . . 13
2.8.3 Bethe–Salpeter equation . . . 14
2.9 Optical properties from the BSE . . . 16

3 Implementation 17

3.1 Momentum matrix elements . . . 17
3.1.1 FV treatment . . . 17
3.1.2 SV treatment . . . 18
3.1.3 SVLO treatment . . . 18
3.2 Plane-wave matrix elements . . . 19
3.2.1 FV treatment . . . 19
3.2.2 SV treatment . . . 20
3.2.3 SVLO treatment . . . 20

3.3 Assembly of the interaction kernel and effective Hamiltonian 21
3.3.1 Use of momentum matrix elements 21
3.3.2 Use of plane-wave matrix elements 21

4 Results **23**
4.1 SVLO-BSE Implementation Verification Criteria 23
4.2 Computational Details 23
4.2.1 Ground State Calculations 24
4.2.2 Excited State Calculations 25
4.3 Optical Spectra 25
4.4 Exciton Energy 26
4.5 MoS_2 26
4.6 PbI_2 30
4.7 $CsPbI_3$ 35
4.8 Cs2PbI4 40
4.9 $Cs_4AgBiBr_8$ 44

5 Conclusion **47**

6 Acknowledgements **53**

1 Introduction

Understanding and predicting the optical properties of materials is of great importance in modern materials science and solid-state physics. In particular, spin–orbit coupling (SOC) may play a crucial role in determining not only the electronic structure but also the optical properties of materials. SOC effects can alter the band gap and induce state mixing. Consequently, SOC-induced orbital mixing can lead to significant changes in a material's optical spectra. This SOC effect is most pronounced in materials containing heavy elements. A representative example is the layered semiconductor lead iodide PbI_2. Due to its direct band gap in the visible region, it is widely used as a precursor for halide perovskite materials [1]. These optical properties are primarily governed by the exciton, a quasi-particle formed by the Coulomb interaction between an excited electron and the resulting hole.

In general, the Bethe–Salpeter equation (BSE), based on many-body perturbation theory, is used to describe these excitons, and its solution provides key insights. The BSE explicitly incorporates electron–hole interactions through an interaction kernel composed of direct and exchange interactions. By solving this two-particle eigenvalue problem, optical spectra can be theoretically predicted with high precision, often agreeing well with experiment [2]. However, the computational cost of the BSE solution, particularly the diagonalisation step, scales as $O(N^3)$ when the BSE Hamiltonian size is $N = N_o N_u N_k$ (occupied $\times$ unoccupied bands $\times$ k-points). Including SOC doubles the number of components per state, increasing this cost by at least a factor of eight, making calculations impractical for many systems of interest [2].

To address these challenges, recent advances in DFT such as the second-variational with local orbitals (SVLO) [3] offer promising solutions. The SVLO method is implemented in the all-electron package `exciting`. Within `exciting`, the linearised augmented plane wave (LAPW) method is employed [4]. In this LAPW framework, core states are solved using the radial four-component Dirac equation, while semicore and valence states are described in the scalar-relativistic (SR) approximation. To efficiently incorporate SOC for these states, a second-variational (SV) method is employed to diagonalise H_{SOC} within a selected SR subspace. First the Kohn–Sham (KS) problem is solved in the SR approximation. Using the SR solutions, a spin-inclusive basis is constructed and the SOC Hamiltonian is solved in this subspace as a perturbation. For many materials this approach can require nearly all available basis vectors to converge. Halide perovskites may require the entire set of KS eigenstates using plain SV [5]. To overcome this, local orbitals (LOs), such as $p_{1/2}$ derived from the full radial Dirac equation, are added in the SV step. These Dirac-type LOs markedly increase basis flexibility in the atomic

regions, and the SVLO method has been shown to greatly enhance efficiency [3].

In this thesis, the SVLO method is extended within the BSE framework of `exciting`. The core implementation concerns two types of matrix elements: momentum matrix elements for transition coefficients proportional to oscillator strength, and plane-wave matrix elements from the Coulomb interaction between Bloch states, which build the BSE interaction kernel [2]. The code design and tests are described below.

2 Theoretical Background

2.1 Density Functional Theory

Density Functional Theory (DFT) is one of the most widely used theoretical methods to calculate the ground state of many-body systems. In order to get the material properties, one must solve the many-body Schrödinger equation involving many nuclei and electrons. However, due to the very high number of interactions of electrons and between electrons and nuclei, in practice it is impossible to find an exact solution of this huge system. Thus, simplifications and approximations in theory are needed. The most fundamental idea of using the density as a basic variable originated with the early statistical models of Thomas [6] and Fermi [7] in the late 1920s. Based on this work, Hohenberg and Kohn [8] established a more rigorous theoretical framework, which ultimately resulted in the viable computational method developed by Kohn and Sham [9]. The basic theoretical framework of DFT will be described in the sections to follow.

2.2 Hohenberg-Kohn theorem

Hohenberg and Kohn established two basic theorems in 1964 [8]:

1. **Uniqueness of External Potential:** The ground-state electron density $n_0(\mathbf{r})$ of an interacting system uniquely determines its external potential $v_{\text{ext}}(\mathbf{r})$.

$$v_{\text{ext}}(\mathbf{r}) = v[n_0(\mathbf{r})] \tag{2.1}$$

   This means that because the external potential is a one-to-one functional of the ground-state density, so is the total Hamiltonian of the system specified by $n_0(\mathbf{r})$. Therefore, all ground-state properties of the system are, in principle, functionals of $n_0(\mathbf{r})$.

2. **Variational Principle for Energy:** For any external potential $v_{\text{ext}}(\mathbf{r})$, there is a universal energy functional, $E[n(\mathbf{r})]$. The actual ground-state energy E_0 of the system is the minimum of the functional for all real $n(\mathbf{r})$ and this minimum occurs if and only if the input density $n(\mathbf{r})$ is the actual ground-state density $n_0(\mathbf{r})$.

$$E_0 = E[n_0(\mathbf{r})] = \min_{n(\mathbf{r})} E[n(\mathbf{r})] \tag{2.2}$$

The energy functional $E[n(\mathbf{r})]$ is expressed as:

$$E[n(\mathbf{r})] = F_{HK}[n(\mathbf{r})] + \int n(\mathbf{r}) v_{\text{ext}}(\mathbf{r}) d\mathbf{r} \tag{2.3}$$

In this case, $F_{HK}[n(\mathbf{r})]$ is a universal functional of the density that does not depend on the particular external potential $v_{\text{ext}}(\mathbf{r})$. It contains the kinetic energy of the interacting electrons and the electron-electron interaction energy.

These two theorems establish the fundamental possibility of dealing with a complicated and interacting many-electron system with only its electron density $n(\mathbf{r})$ as the fundamental variable, rather than the much more complex many-body wavefunction.

2.3 Kohn-Sham equation

Following the Hohenberg-Kohn theorems, Kohn and Sham proposed an auxiliary non-interacting system that will reproduce the ground-state density of the actual, interacting system [9]. These theorems for a non-interacting system are the basis of the DFT calculations. The Kohn-Sham equation takes the form of a single-particle Schrödinger equation:

$$\left[-\frac{\hbar^2}{2m} \nabla^2 + v_{\text{eff}}(\mathbf{r}) \right] \phi_i(\mathbf{r}) = \epsilon_i \phi_i(\mathbf{r}) \tag{2.4}$$

Here, $\phi_i(\mathbf{r})$ is the single-particle wavefunction, also known as a Kohn-Sham orbital and ϵ_i is the respective Kohn-Sham energy of the i-th orbital. The ground-state electron density $n(\mathbf{r})$ of the interacting system is built up from these Kohn-Sham orbitals as follows:

$$n(\mathbf{r}) = \sum_{i}^{\text{occ}} |\phi_i(\mathbf{r})|^2 \tag{2.5}$$

The summation runs over all the occupied Kohn-Sham orbitals.

A key component of the Kohn-Sham approach is the effective potential, $v_{\text{eff}}(\mathbf{r})$. This potential consists of the following three terms:

$$v_{\text{eff}}(\mathbf{r}) = v_{\text{ext}}(\mathbf{r}) + v_{\text{Hartree}}(\mathbf{r}) + v_{\text{xc}}(\mathbf{r}) \tag{2.6}$$

Here, $v_{\text{ext}}(\mathbf{r})$ is the external potential, and $v_{\text{Hartree}}(\mathbf{r})$ is the Hartree potential which is the classical electrostatic repulsion of the electrons and is given by:

$$v_{\text{Hartree}}(\mathbf{r}) = e^2 \int \frac{n(\mathbf{r}')}{|\mathbf{r} - \mathbf{r}'|} d\mathbf{r}' \tag{2.7}$$

Finally, $v_{\text{xc}}(\mathbf{r})$ is the exchange-correlation potential which captures all quantum mechanical many-body effects such as electronic exchange and correlation that go beyond the classical

Hartree potential. It is given by the functional derivative of the exchange-correlation energy functional, $E_{\text{xc}}[n(\mathbf{r})]$, with respect to the density:

$$v_{\text{xc}}(\mathbf{r}) = \frac{\delta E_{\text{xc}}[n(\mathbf{r})]}{\delta n(\mathbf{r})} \tag{2.8}$$

The exact functional form of the exchange-correlation energy, $E_{\text{xc}}[n]$, from which $v_{\text{xc}}(\mathbf{r})$ is derived, is not known. Therefore, different approximations to the degree of $E_{\text{xc}}[n]$ have been established. The reliability of DFT calculations depends significantly on the quality of the exchange-correlation functional used. The most basic approximation level is the local density approximation (LDA) [9], where one assumes that the exchange-correlation energy at some point $\mathbf{r}$ is a function of the electron density $n(\mathbf{r})$ at that very point, as in a uniform electronic gas. It is typically represented as the exchange-correlation energy per particle of a homogeneous electron gas, $\epsilon_{\text{xc}}^{\text{hom}}(n)$:

$$E_{\text{xc}}^{\text{LDA}}[n(\mathbf{r})] = \int n(\mathbf{r})\epsilon_{\text{xc}}^{\text{hom}}(n(\mathbf{r}))d\mathbf{r} \tag{2.9}$$

Due to the limitations imposed by this rough assumption, more advanced approximations such as the generalized gradient approximation (GGA) are developed [10]. The GGA functional is typically written as:

$$E_{\text{xc}}^{\text{GGA}}[n(\mathbf{r}), \nabla n(\mathbf{r})] = \int f(n(\mathbf{r}), |\nabla n(\mathbf{r})|)d\mathbf{r} \tag{2.10}$$

Here, the functional depends not just on the local density $n(\mathbf{r})$ itself but also on its gradient, $\nabla n(\mathbf{r})$, in general, giving a more realistic description of inhomogeneous interacting systems. One of the most popular GGA functionals is the Perdew-Burke-Ernzerhof (PBE) functional [10] that for most purposes gives an optimal balance between accuracy and computational expense. The Kohn-Sham equations (2.4) have to be solved self-consistently. This is because the electron density $n(\mathbf{r})$ (2.5) is a function of the Kohn-Sham orbitals $\phi_i(\mathbf{r})$, while the effective potential $v_{\text{eff}}(\mathbf{r})$ (2.6) in turn depends on $n(\mathbf{r})$. DFT is a very powerful theoretical technique whereby a complex interacting many-body problem may be mapped onto a solvable problem of non-interacting fictitious particles moving in an effective potential.

2.4 Linearized Augmented Planewave Method

For periodic systems, such as crystals, the Kohn-Sham equation for an electron with wave vector $\mathbf{k}$ in band n is typically written in Bloch form as [11] :

$$\hat{H}_{\text{KS}}\psi_{n\mathbf{k}}(\mathbf{r}) = \left[-\frac{\hbar^2}{2m}\nabla^2 + v_{\text{eff}}(\mathbf{r})\right]\psi_{n\mathbf{k}}(\mathbf{r}) = \epsilon_{n\mathbf{k}}\psi_{n\mathbf{k}}(\mathbf{r}) \tag{2.11}$$

where $\psi_{n\mathbf{k}}(\mathbf{r})$ are the Kohn-Sham orbitals expressed as Bloch wavefunctions satisfying periodic condition, $\psi_{n\mathbf{k}}(\mathbf{r}+\mathbf{R}) = e^{i\mathbf{k}\cdot\mathbf{R}}\psi_{n\mathbf{k}}(\mathbf{r})$ for any lattice vector $\mathbf{R}$ and $\epsilon_{n\mathbf{k}}$ are the corresponding Kohn-Sham energy eigenvalues. Solving this equation is a crucial step in addressing many modern solid-state physics problems. The first step in solving this equation involves choosing an appropriate way to represent the electronic wavefunctions $\psi_{n\mathbf{k}}(\mathbf{r})$. To accurately describe the wavefunction, the chosen representation must account for its different behaviors in distinct spatial regions of the crystal [12]. In the vicinity of the atomic nuclei, the wavefunction oscillates rapidly, while in the interstitial regions between atoms, it typically varies more smoothly. While various approximation schemes exist, one common and highly accurate approach is to partition the unit cell into two distinct regions, with the wavefunctions being represented differently in each region. The first region consists of non-overlapping spheres, known as muffin-tin (MT) spheres with a radius $R_{\mathrm{MT},\alpha}$ centered on each atom α. The second region is the interstitial (I) space, which is the volume between these atomic spheres. In this dual representation, the basis functions, $\phi_{\mathbf{k}+\mathbf{G}}(\mathbf{r})$, are defined as follows [4]:

$$\phi_{\mathbf{k}+\mathbf{G}}(\mathbf{r}) = \begin{cases} \sum_{l=0}^{l_{\max}} \sum_{m=-l}^{l} \left[A_{lm}^{\alpha}(\mathbf{k}+\mathbf{G})u_{l\alpha}(r_\alpha, E_{l\alpha}) + B_{lm}^{\alpha}(\mathbf{k}+\mathbf{G})\dot{u}_{l\alpha}(r_\alpha, E_{l\alpha})\right] Y_{lm}(\hat{\mathbf{r}}_\alpha) & \text{if } r_\alpha \leq R_{\mathrm{MT},\alpha} \\ \frac{1}{\sqrt{\Omega}} e^{i(\mathbf{k}+\mathbf{G})\cdot\mathbf{r}} & \text{if } \mathbf{r} \in \mathrm{I} \end{cases} \tag{2.12}$$

Here, $r_\alpha = |\mathbf{r} - \mathbf{R}_\alpha|$ is the distance from the nucleus of the atom α, Ω is the unit cell volume, $Y_{lm}(\hat{\mathbf{r}}_\alpha)$ are spherical harmonics and $u_{l\alpha}(r_\alpha, E_{l\alpha})$ are numerical radial functions evaluated at the fixed linearization energy $E_{l\alpha}$. The term $\dot{u}_{l\alpha}(r_\alpha, E_{l\alpha}) = \frac{\partial u_{l\alpha}(r_\alpha, E)}{\partial E}\Big|_{E=E_{l\alpha}}$ is the energy derivative of this radial function. The coefficients $A_{lm}^{\alpha}(\mathbf{k}+\mathbf{G})$ and $B_{lm}^{\alpha}(\mathbf{k}+\mathbf{G})$ are determined by requiring that the basis function and its radial derivative are continuous at the MT sphere boundary with matching the interstitial plane wave. Within each MT sphere, $u_{l\alpha}$ is obtained from the *scalar-relativistic* Kohn–Sham radial equation in the spherically averaged potential $V_0^{\alpha}(r_\alpha)$ at the energy $E_{l\alpha}$:

$$\left[-\frac{\hbar^2}{2m}\frac{1}{r_\alpha^2}\frac{d}{dr_\alpha}\left(r_\alpha^2\frac{d}{dr_\alpha}\right) + \frac{\hbar^2 l(l+1)}{2mr_\alpha^2} + V_0^{\alpha}(r_\alpha) - E_{l\alpha}\right] u_{l\alpha}(r_\alpha, E_{l\alpha}) = 0 \tag{2.13}$$

This method is called the Augmented Plane Wave (APW) method. In the APW method, the radial functions $u_{l\alpha}$ depend explicitly on the eigenenergy $\epsilon_{n\mathbf{k}}$ of the state leading to a non-linear eigenvalue problem. To overcome this and construct an energy-independent basis set, the Linearized Augmented Plane Wave (LAPW) method, as expressed in Eq. (2.12), utilizes both $u_{l\alpha}(r_\alpha, E_{l\alpha})$ and its energy derivative $\dot{u}_{l\alpha}(r_\alpha, E_{l\alpha})$ at fixed linearization energies $E_{l\alpha}$ [13]. This approach effectively linearizes the energy dependence of the radial wave function within the energy window of interest around $E_{l\alpha}$, following a first-order Taylor expansion:

$$u_{l\alpha}(r_\alpha, E) \approx u_{l\alpha}(r_\alpha, E_{l\alpha}) + (E - E_{l\alpha})\dot{u}_{l\alpha}(r_\alpha, E_{l\alpha}) \tag{2.14}$$

Using this set of fixed-energy radial functions ($u_{\ell\alpha}$ and $\dot{u}_{\ell\alpha}$), the explicit dependence of the basis on the eigenvalue is removed, and the nonlinear secular equation reduces to the generalized linear eigenvalue problem:

$$\sum_{\mathbf{G}'} H^{\mathbf{k}}_{\mathbf{G}\mathbf{G}'}\, c_{n\mathbf{k}}(\mathbf{G}') \;=\; \epsilon_{n\mathbf{k}} \sum_{\mathbf{G}'} S^{\mathbf{k}}_{\mathbf{G}\mathbf{G}'}\, c_{n\mathbf{k}}(\mathbf{G}'), \tag{2.15}$$

where $H^{\mathbf{k}}_{\mathbf{G}\mathbf{G}'}$ and $S^{\mathbf{k}}_{\mathbf{G}\mathbf{G}'}$ are the Hamiltonian and overlap matrix elements in the LAPW basis, respectively, and $c_{n\mathbf{k}}(\mathbf{G}')$ are the expansion coefficients of the Kohn–Sham orbital $\psi_{n\mathbf{k}}$.

The flexibility of the LAPW basis can be further improved by additionally introducing basis functions, called local orbitals [14]. These additional basis functions are non-zero only within selected muffin-tin spheres. They are designed to improve the description of particular states and they will be discussed in the following section.

2.5 Local Orbital

These local orbitals are constructed from linear combinations of radial functions evaluated at linearization energies $E_{l\alpha,j}$ and they are defined to be zero in the interstitial region. A general mathematical form for an LO, identified by a composite index μ , centered on atom α are expressed as:

$$\phi^{\mu}_{\mathrm{LO}}(\mathbf{r}) = \begin{cases} \left[\sum_{j=1}^{N^{\mu}_{\mathrm{LO}}} C^{\mu}_{j} u^{(j)}_{l\alpha}(r_\alpha, E_{l\alpha,j})\right] Y_{lm}(\hat{\mathbf{r}}_\alpha) & \text{if } r_\alpha \le R_{\mathrm{MT},\alpha} \\ 0 & \text{if } \mathbf{r} \in \mathrm{I} \end{cases} \tag{2.16}$$

The coefficients C^{μ}_{j}, along with the choice of linearization energies $E_{l\alpha,j}$ and the types of radial functions $u^{(j)}_{l\alpha}$ used in the sum in Eq. (2.16) are determined by imposing specific conditions. These typically include ensuring the LO and its radial derivative vanish at the MT sphere boundary, and normalization of the LO within the sphere.

The main motivation for introducing these LOs is to enhance the description of semicore states that may not be adequately represented by the standard (L)APW basis alone and to more accurately capture relativistic effects, which are typically pronounced near the atomic nuclei.

Typically, LOs can be used to accurately represent semi-core states, which are too high in energy to be treated as core states but too localized to be well-described by the valence linearization energies or they can be used to provide additional variational freedom for the valence states themselves, especially for orbitals with strong atomic character [14],[4],[3].

2.6 Dirac Type Local Orbital

As mentioned earlier, local orbitals are used to improve the completeness of the basis set in the core region. The influence of spin–orbit coupling (SOC) is particularly pronounced near

atomic nuclei, leading to significant changes in the electronic band structure. For example, band splitting occurs, and this phenomenon is especially strong in materials containing heavy elements. This splitting signifies a transition from a description based on the orbital angular momentum quantum number l and the spin component s to a description based on the total angular momentum quantum number $j = l \pm s$ (for electrons $s = \frac{1}{2}$). Radial wave functions dependent on j, which exhibit significantly different short-range (near-nucleus) behavior compared to their scalar-relativistic counterparts, are obtained as solutions to the Dirac equation rather than the scalar-relativistic Schrödinger equation. This difference in behavior is visually represented in Figure 2.1.

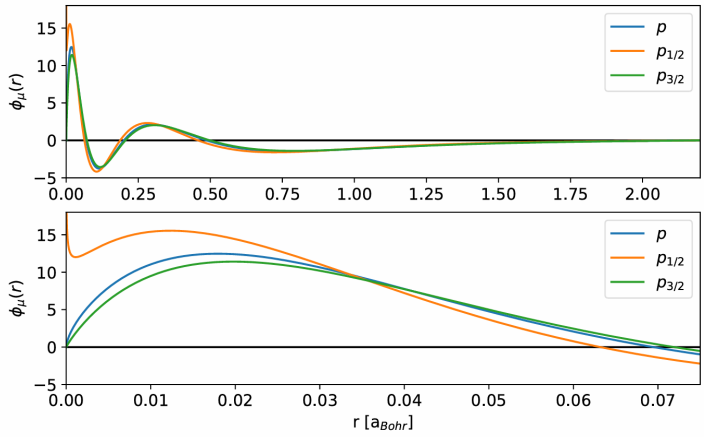

Figure 2.1: Comparison of the radial behavior of p-type orbitals for Pb: scalar-relativistic (SR) vs. Dirac-type ($p_{1/2}$ and $p_{3/2}$). Note the distinct behavior near the nucleus for the Dirac-type functions. For more discussion, see [15].

To accurately capture these relativistic effects within the (L)APW+lo basis set, Dirac-type local orbitals (LOs) are introduced. The radial part of such an LO, $U_\mu^{\text{Dirac}}(r_\alpha)$, is written as a linear combination of numerical solutions of the radial Dirac equation,

$$U_\mu^{\text{Dirac}}(r_\alpha) = \sum_\xi C_{\mu\xi}\, u_{\alpha\xi lj}(r_\alpha; \epsilon_{\alpha\xi lj}), \tag{2.17}$$

where α labels the atomic site, l and j are the orbital and total angular-momentum quantum numbers, and ξ enumerates different choices of energy parameters for the same pair (l, j); the radial functions $u_{\alpha\xi lj}$ are evaluated at the specific energies $\epsilon_{\alpha\xi lj}$. The coefficients $C_{\mu\xi}$ are determined by boundary and normalization conditions for the LO.

This construction differs from standard LOs that typically use solutions of a scalar-relativistic (SR) radial equation. An SR LO has radial part $U_{\mu'}^{\text{SR}}(r_\alpha)$ formed from solutions $u_{\alpha\xi l}(r_\alpha; \epsilon_{\alpha\xi l})$ depending only on l:

$$U_\mu^{\text{SR}}(r_\alpha) = \sum_\xi C_{\mu\xi}\, u_{\alpha\xi l}(r_\alpha; \epsilon_{\alpha\xi l}), \tag{2.18}$$

with μ indexing the SR LO and $C_{\mu\xi}$ the corresponding coefficients. The key difference is that

$u_{\alpha\xi lj}$ in Eq. (2.17) are solutions of the Dirac equation and hence explicitly j-dependent, whereas $u_{\alpha\xi l}$ in Eq. (2.18) are solutions of an SR equation and are only l-dependent.

By employing radial functions derived directly from the Dirac equation, Dirac-type LOs provide a more accurate representation of the near-nucleus behavior and the j-dependence, thereby improving the description of strong-SOC materials [3, 15, 16].

2.7 Relativistic Treatment

As previously discussed, accurately accounting for relativistic effects, particularly spin-orbit coupling, is critical for a precise description of the electronic structure and optical properties of many materials, especially those containing heavy atoms. The starting point for incorporating these effects within a Kohn-Sham framework is often the two-component Kohn-Sham equation, which explicitly includes spin components. For a given k-point and band index n, this equation can be written as:

$$\sum_{\sigma'=\uparrow,\downarrow} \hat{H}_{\sigma\sigma'}(\mathbf{k})\Psi_{n\mathbf{k}\sigma'}(\mathbf{r}) = \epsilon_{n\mathbf{k}}\Psi_{n\mathbf{k}\sigma}(\mathbf{r}) \tag{2.19}$$

Here, $\Psi_{n\mathbf{k}\sigma}(\mathbf{r})$ represents the σ-spin component of the two-component spinor wavefunction $\Psi_{n\mathbf{k}}(\mathbf{r}) = \sum_\sigma \Psi_{n\mathbf{k}\sigma}(\mathbf{r})|\sigma\rangle$, and $\epsilon_{n\mathbf{k}}$ is the corresponding Kohn-Sham eigenvalue. The Hamiltonian operator $\hat{H}_{\sigma\sigma'}(\mathbf{k})$ includes both scalar-relativistic (SR) contributions and the spin-orbit coupling (SOC) term[3]:

$$\hat{H}_{\sigma\sigma'}(\mathbf{k}) = \delta_{\sigma\sigma'}\hat{H}^{\mathrm{SR}}_{\sigma}(\mathbf{k}) + \hat{H}^{\mathrm{SOC}}_{\sigma\sigma'}(\mathbf{k}) \tag{2.20}$$

Based on this fundamental equation, several distinct approaches have been developed to perform electronic structure calculations incorporating relativistic effects[17]. These methods vary in their level of approximation and computational cost, and will be discussed in the following subsections.

2.7.1 Non-Perturbative Treatment

The most direct and, in principle, most accurate approach to solving Eq. (2.19) is the non-perturbative (NP) treatment. This method involves directly diagonalizing the full two-component Hamiltonian given by Eq. (2.20), thereby treating the scalar-relativistic terms and the SOC term on an equal footing. By explicitly including the spin components throughout the calculation, the size of the basis set effectively doubles compared to a spin-restricted scalar-relativistic calculation, from N_b to $2N_b$ basis functions if each original basis function gives rise to two spin components. Consequently, the computational cost of diagonalizing the Kohn-Sham Hamiltonian, which typically scales with the cube of the basis set size, increases significantly, approximately to $O((2N_b)^3) = O(8N_b^3)$. While providing the most accurate treatment of SOC, this high computational demand can make NP calculations prohibitive for large or complex systems[17, 18].

2.7.2 Scalar-Relativistic Treatment

The scalar-relativistic (SR) treatment offers a simplified approach by considering only the SR part of the Hamiltonian, $\hat{H}_{\sigma}^{\mathrm{SR}}(\mathbf{k})$, from Eq. (2.20), and neglecting the explicit spin-orbit coupling term $\hat{H}_{\sigma\sigma'}^{\mathrm{SOC}}(\mathbf{k})$. The SR Hamiltonian itself is derived by simplifying the full four-component Dirac equation, retaining the mass-velocity and Darwin terms, but omitting terms that directly couple spin and orbital motion. For more detail, see [16] and [4]. Essentially, the SR calculation solves the following Kohn-Sham-like equation for each spin component σ independently :

$$\hat{H}_{\sigma}^{\mathrm{SR}}(\mathbf{k})\Psi_{j\mathbf{k}\sigma}^{\mathrm{FV}}(\mathbf{r}) = \epsilon_{j\mathbf{k}\sigma}^{\mathrm{FV}}\Psi_{j\mathbf{k}\sigma}^{\mathrm{FV}}(\mathbf{r}) \tag{2.21}$$

Here, $\Psi_{j\mathbf{k}\sigma}^{\mathrm{FV}}(\mathbf{r})$ are the so-called first-variational (FV) Kohn-Sham orbitals obtained from the SR approximation, with corresponding eigenvalues $\epsilon_{j\mathbf{k}\sigma}^{\mathrm{FV}}$. Within the (L)APW+lo method, these FV wavefunctions are expanded in the (L)APW+lo basis (as described in Section 2.4, combining $\phi_{\mathbf{G}+\mathbf{k}}(\mathbf{r})$ and LOs $\phi_{\mu}(\mathbf{r})$):

$$\Psi_{j\mathbf{k}\sigma}^{\mathrm{FV}}(\mathbf{r}) = \sum_{\mathbf{G}} C_{\mathbf{k}\sigma\mathbf{G}j}\phi_{\mathbf{G}+\mathbf{k}}(\mathbf{r}) + \sum_{\mu} C_{\mathbf{k}\sigma\mu j}\phi_{\mu}(\mathbf{r}) \tag{2.22}$$

Since explicit spin-orbit coupling and thus the coupling between spin components are not included at this stage, the number of basis functions needed for a given spatial orbital is N_b, leading to a computational cost that scales roughly $O(N_b^3)$. This approach is computationally less demanding than the NP method but does not capture SOC-induced phenomena like band splitting[3, 17, 18].

2.7.3 Second Variational Treatment

Despite the high accuracy of the NP method, its computational cost motivates alternative approaches such as the second variational (SV) treatment. The main idea behind the SV method is to treat the SOC term, $\hat{H}_{\sigma\sigma'}^{\mathrm{SOC}}(\mathbf{k})$, as a perturbation acting on the eigenstates obtained from a scalar-relativistic calculation. The SV procedure is typically composed of two steps:

1. First, the SR Kohn-Sham equation (2.21) is solved to obtain the set of SR eigenfunctions $\Psi_{j\mathbf{k}\sigma}^{\mathrm{FV}}(\mathbf{r})$ and eigenvalues $\epsilon_{j\mathbf{k}\sigma}^{\mathrm{FV}}$.

2. Secondly, a selected subset of these SR eigenfunctions $\left\{\Psi_{j\mathbf{k}\sigma}^{\mathrm{FV}}(\mathbf{r})\right\}$ is used to construct a new basis set that explicitly includes spin. The SOC Hamiltonian is then diagonalized within this new basis. The resulting spin-inclusive wavefunctions $\Psi_{n\mathbf{k}}^{\mathrm{SV}}(\mathbf{r})$ are expressed as linear combinations of the SR FV states, now coupled by SOC:

$$\Psi_{n\mathbf{k}}^{\mathrm{SV}}(\mathbf{r}) = \sum_{\sigma,j} C_{\mathbf{k}\sigma jn}^{\mathrm{SV}}\Psi_{j\mathbf{k}\sigma}^{\mathrm{FV}}(\mathbf{r})|\sigma\rangle \tag{2.23}$$

In the sum over j, typically all occupied SR states (N_{occ}) are included, while only a limited number of unoccupied SR states (N_{unocc}) are used to form the basis for the SV step. The inclusion of all occupied states is often crucial for accurately capturing effects in the core and near-nuclear regions. With this basis, one solves the orthogonal eigenvalue problem for the expansion coefficients $C^{\text{SV}}_{\mathbf{k}\sigma jn}$:

$$\sum_{\sigma' j'} \langle \Psi^{\text{FV}}_{j\mathbf{k}\sigma} | \hat{H}_{\sigma\sigma'}(\mathbf{k}) | \Psi^{\text{FV}}_{j'\mathbf{k}\sigma'} \rangle C^{\text{SV}}_{\mathbf{k}\sigma' j' n} = \epsilon^{\text{SV}}_{n\mathbf{k}} \sum_{\sigma' j'} \langle \Psi^{\text{FV}}_{j\mathbf{k}\sigma} | \Psi^{\text{FV}}_{j'\mathbf{k}\sigma'} \rangle C^{\text{SV}}_{\mathbf{k}\sigma' j' n} \tag{2.24}$$

The computational cost of this two-step procedure scales as $O(N_b^3) + O((2N_{\text{SV}})^3)$, where $N_{\text{SV}} = N_{\text{occ}} + N_{\text{unocc}}$ is the size of the SR eigenfunction subspace used in the second step. If $N_{\text{SV}} \ll N_b$, this method can be significantly more efficient than the NP approach [3, 17, 18].

2.7.4 Second Variation with Local Orbital Method

Despite the computational advantages of the SV method for many systems, problems can arise, particularly when SOC is too strong to be accurately treated as a small perturbation. In such cases, achieving convergence with the SV method might require including almost all unoccupied SR states, $N_{\text{unocc}} \approx N_b - N_{\text{occ}}$, making N_{SV} comparable to N_b. This diminishes the computational efficiency gain over the NP method. Furthermore, the standard SV method, relying solely on SR eigenfunctions, may not be flexible enough to accurately represent the changes in wavefunction character induced by SOC, particularly the behavior of local orbitals near the atomic nuclei. For these reasons, the second variation with local orbitals (SVLO) method was introduced [3].

The fundamental idea of SVLO is to enhance the basis set used in the second variational step by explicitly including local orbitals in addition to the SR eigenfunctions. This provides greater variational freedom, especially for describing SOC effects that are strongly localized near the atomic nuclei. The SVLO procedure can be outlined as follows:

1. First, as in the SV method, the SR Kohn-Sham equation (2.21) is solved using the (L)APW+lo basis to obtain SR eigenfunctions $\Psi^{\text{FV}}_{j\mathbf{k}\sigma}(\mathbf{r})$ (defined in Eq. (2.22)).

2. To avoid linear dependency issue when combining SR eigenfunctions with the original LOs, the LO contributions are removed from the SR eigenfunctions used in the SVLO basis. This results in modified FV wavefunctions, $\bar{\Psi}^{\text{FV}}_{j\mathbf{k}\sigma}(\mathbf{r})$, which primarily contain the (L)APW character:
$$\bar{\Psi}^{\text{FV}}_{j\mathbf{k}\sigma}(\mathbf{r}) = \sum_{\mathbf{G}} C_{\mathbf{k}\sigma\mathbf{G}j} \phi_{\mathbf{G}+\mathbf{k}}(\mathbf{r}) \tag{2.25}$$

3. A new, extended basis set for the second variational step is then constructed by combining these modified SR eigenfunctions $\bar{\Psi}^{\text{FV}}_{j\mathbf{k}\sigma}(\mathbf{r})$ with the original set of local orbitals $\phi_\mu(\mathbf{r})$ (including standard LOs and potentially Dirac-type LOs, as discussed in Section 2.6. The

SVLO spinor wavefunction $\Psi^{\text{SVLO}}_{n\mathbf{k}}(\mathbf{r})$ is then expressed as:

$$\Psi^{\text{SVLO}}_{n\mathbf{k}}(\mathbf{r}) = \sum_{\sigma,j} C^{\text{SVLO}}_{\mathbf{k}\sigma jn} \bar{\Psi}^{\text{FV}}_{j\mathbf{k}\sigma}(\mathbf{r})|\sigma\rangle + \sum_{\sigma,\mu} C^{\text{SVLO}}_{\mathbf{k}\sigma\mu n} \phi_\mu(\mathbf{r})|\sigma\rangle \tag{2.26}$$

By doing this, the total number of basis functions $N_b^{\text{SV(LO)}}$ used in the second step for the SV and SVLO methods can be compared:

$$N_b^{\text{SV(LO)}} = \begin{cases} N_{\text{occ}} + N_{\text{unocc}} & \text{for SV} \\ N_{\text{occ}} + N_{\text{unocc}} + N_{\text{LO}} & \text{for SVLO} \end{cases} \tag{2.27}$$

In calculations, N_{unocc} is a computational parameter that needs to be converged for both methods. The SVLO method aims to achieve convergence with a much smaller N_{unocc} due to the explicit inclusion of N_{LO} physically relevant local orbitals. With a relatively small number of well-chosen LOs, particularly Dirac-type LOs that accurately capture near-nucleus relativistic behavior, the SVLO method can achieve convergence much faster and often with better accuracy than the conventional SV method, especially for materials with strong SOC. More details on the performance and specific construction of LOs within SVLO are provided in the work by Vona et al. [3].

2.8 Many-Body Perturbation Theory

While Density Functional Theory (DFT) provides an efficient description of ground-state properties, neutral optical excitations and electron–hole interaction are most naturally formulated within Many-Body Perturbation Theory (MBPT) using the screened Coulomb interaction and an effective electron–hole kernel [19, 20].

2.8.1 Screened Coulomb interaction in MBPT

The only MBPT quantity explicitly entering our optical formulation is the screened Coulomb interaction W, defined through the inverse dielectric function as in Eq. (2.31). In practice, the static limit $W(\omega = 0)$ is employed for near-gap spectra [2, 19]. At the level needed for the Bethe–Salpeter equation (BSE), the interaction kernel is used in the standard static, Hermitian decomposition

$$K = K^{\text{dir}} + K^{x},$$

where K^{dir} is an attractive term built from W and K^x is a repulsive exchange term constructed from the bare Coulomb interaction v_c [2, 20]. This decomposition underlies the electron–hole Hamiltonian and fixes the sign conventions and notation used in the following BSE formulas [19]. Note that sign conventions for K^{dir} and K^x can differ in the literature; here we follow the convention of Refs. [2, 20].

As useful limiting cases within this framework, three levels will be referenced throughout: (i) the independent-particle picture with $K = 0$; (ii) the random-phase approximation retaining local-field effects via K^x while setting $K^{\mathrm{dir}} = 0$; and (iii) the full singlet BSE including both K^{dir} and K^x, which captures bound excitons and near-edge lineshapes [2, 20].

All matrix elements, the key ingredients for the BSE, entering K^{dir} and K^x are evaluated using spinor wavefunctions, consistent with the SOC treatment employed in the implementation[2].

2.8.2 Dielectric Function

The way that a material reacts to an external electric field is fundamentally governed by its dielectric properties [2]. Within the linear response theory, the electric displacement field $\mathbf{D}(\mathbf{r}, \omega)$ in a material is proportional to the externally applied electric field $\mathbf{E}(\mathbf{r}, \omega)$. The proportionality is determined by the dielectric tensor $\epsilon_{ij}(\mathbf{r}, \mathbf{r}', \omega)$ that is defined as:

$$D_i(\mathbf{r}, \omega) = \int d^3\mathbf{r}' \epsilon_{ij}(\mathbf{r}, \mathbf{r}', \omega) E_j(\mathbf{r}', \omega) \tag{2.28}$$

It is this equation that explains the overall linear response of the system to a global electromagnetic perturbation. The dielectric tensor is usually reformulated in terms of the total polarization function $P_{ij}(\mathbf{r}, \mathbf{r}', \omega)$, a description of the change in the charge density in response to a total potential. The inverse dielectric tensor ϵ_{ij}^{-1} can be expressed in terms of the polarization P_{ij} and the bare Coulomb interaction $v_c(\mathbf{r} - \mathbf{r}')$ as:

$$\epsilon_{ij}^{-1}(\mathbf{r}, \mathbf{r}', \omega) = \delta_{ij}\delta(\mathbf{r} - \mathbf{r}') + \int d^3\mathbf{r}'' v_c(\mathbf{r} - \mathbf{r}'') P_{ij}(\mathbf{r}'', \mathbf{r}', \omega) \tag{2.29}$$

It is useful for systems exhibiting translational symmetry such as crystals, to transform the dielectric tensor to reciprocal space via a Fourier transform. The dielectric tensor in real space may be written in terms of its Fourier components $\epsilon_{ij,\mathbf{GG}'}(\mathbf{q}, \omega)$, where $\mathbf{q}$ is a wavevector within the first Brillouin zone and $\mathbf{G}, \mathbf{G}'$ are reciprocal lattice vectors:

$$\epsilon_{ij}(\mathbf{r}, \mathbf{r}', \omega) = \frac{1}{\Omega} \sum_{\mathbf{q}} \sum_{\mathbf{G},\mathbf{G}'} e^{i(\mathbf{q}+\mathbf{G})\cdot\mathbf{r}} \epsilon_{ij,\mathbf{GG}'}(\mathbf{q}, \omega) e^{-i(\mathbf{q}+\mathbf{G}')\cdot\mathbf{r}'} \tag{2.30}$$

where Ω is the volume of the unit cell.

The macroscopic dielectric function $\epsilon_M(\omega)$ is obtained from these microscopic entities, usually as the reciprocal of the $(\mathbf{G} = 0, \mathbf{G}' = 0)$ element of the inverse dielectric matrix in the long-wavelength limit ($\mathbf{q} \to 0$). The imaginary part of $\epsilon_M(\omega)$ is straightforwardly connected with the optical absorption spectrum, and its real part is responsible for dispersion and reflection effects. Furthermore, in many-body theory, screening effects need to be incorporated, wherein the interaction between charged particles is altered by the presence of other polarizable electrons in the material. This is described by the dynamically screened Coulomb interaction $W(\mathbf{r}, \mathbf{r}', \omega)$

which is connected to the bare Coulomb interaction v_c and the inverse dielectric function:

$$W(\mathbf{r}, \mathbf{r}', \omega) = \int d^3\mathbf{r}'' \epsilon^{-1}(\mathbf{r}, \mathbf{r}'', \omega) v_c(\mathbf{r}'' - \mathbf{r}') \tag{2.31}$$

This screened interaction W is an essential ingredient of the Bethe–Salpeter equation to describe electron-hole interactions. See [21, 22] for further discussion.

2.8.3 Bethe–Salpeter equation

Although the dielectric function gives a macroscopic description of optical response, a more advanced theoretical model is used to describe particular excited states called excitons.

The optical properties near the absorption edge of materials are usually dominated by excitons, quasiparticles created by the Coulomb interaction of an excited electron and the resulting hole. Unlike independent particle approximations like DFT, which do not deal with such electron-hole interactions explicitly, the Bethe–Salpeter equation (BSE) is a formal method for dealing with these interactions and therefore a cornerstone of MBPT for the study of optical excitations [2]. The BSE is formally a two-particle Schrödinger equation for an electron-hole pair. Solving it gives the excitonic energies Ω^λ and the respective exciton wavefunction amplitudes $A^\lambda_{vc\mathbf{k}}$. In these, v and c are valence and conduction band indices, respectively, $\mathbf{k}$ is the wavevector, and λ is the excitonic state index. The BSE is in the form of the following excitonic eigenvalue problem:

$$\sum_{v'c'\mathbf{k}'} H^{\mathrm{BSE}}_{vc\mathbf{k},v'c'\mathbf{k}'} A^\lambda_{v'c'\mathbf{k}'} = \Omega^\lambda A^\lambda_{vc\mathbf{k}} \tag{2.32}$$

Here, $E^{\mathrm{QP}}_{c\mathbf{k}}$ and $E^{\mathrm{QP}}_{v\mathbf{k}}$ denote the conduction- and valence-band quasiparticle energies, typically taken from GW calculations or approximated from DFT Kohn-Sham energies through a scissor correction. The second term, $K_{vc\mathbf{k},v'c'\mathbf{k}'}$, is the interaction kernel, and it represents the heart of the BSE since it displays the electron-hole interaction. The kernel typically comprises two contributions:

$$K_{vc\mathbf{k},v'c'\mathbf{k}'} = K^{\mathrm{dir}}_{vc\mathbf{k},v'c'\mathbf{k}'} + K^{\mathrm{x}}_{vc\mathbf{k},v'c'\mathbf{k}'} \tag{2.33}$$

The first term, K^{dir}, is the attractive direct screened Coulomb interaction, mediated by W (from Eq. (2.31)), responsible for exciton binding. The second term, K^{x}, is the repulsive bare Coulomb exchange interaction, v_c, arising from the Pauli exclusion principle. It is this term that is accountable for the singlet-triplet exciton splitting and the redistribution of the oscillator strength. Solving the BSE (2.32) yields exciton energies and eigenvectors that govern near-edge absorption and lineshape and are essential to understanding the optical response[2, 21, 22].

2.8.3.1 BSE Hamiltonian

As shown in Eq. (2.34), the BSE Hamiltonian is written as the sum of a diagonal contribution and an interaction kernel:

$$\hat{H}^{\mathrm{BSE}} \;=\; \hat{H}^{\mathrm{diag}} \;+\; \hat{K}. \tag{2.34}$$

The diagonal part collects the quasiparticle energy differences,

$$\left(\hat{H}^{\mathrm{diag}}\right)_{vc\mathbf{k},\,v'c'\mathbf{k}'} \;=\; \delta_{vv'}\,\delta_{cc'}\,\delta_{\mathbf{k}\mathbf{k}'}\left(E^{\mathrm{QP}}_{c\mathbf{k}} - E^{\mathrm{QP}}_{v\mathbf{k}}\right). \tag{2.35}$$

The interaction kernel is used in the standard static, Hermitian decomposition[2, 22] :

$$\hat{K} \;=\; K^{\mathrm{dir}} \;+\; K^{x}. \tag{2.36}$$

2.8.3.2 Independent Particle Approximation

If we neglect the electron-hole interaction kernel $\hat{K}$, the BSE simplifies to the Independent Particle (IP) approximation. Here, the excitonic energies Ω^{λ} are just valence and conduction band quasiparticle energy differences, $\Omega^{\lambda} = E^{\mathrm{QP}}_{c\mathbf{k}} - E^{\mathrm{QP}}_{v\mathbf{k}}$. This fails to account for bound excitonic states below the quasiparticle gap and tends to distort the shape and intensity of the optical spectrum of insulators and semiconductors[2, 21].

2.8.3.3 Electron-Hole Interaction Kernel

The electron-hole interaction kernel, $\hat{K}$, is a crucial ingredient in the excitonic property description within the Bethe–Salpeter equation (BSE) approach. It comprises an attractive direct term K^{dir} and a repulsive exchange term K^{x}. The direct term is built from the screened Coulomb interaction W as in Eq. (2.31), with matrix elements:

$$K^{\mathrm{dir}}_{vc\mathbf{k},v'c'\mathbf{k}'} = -\sum_{\mathbf{G},\mathbf{G}'}\left(M^{\mathbf{G}}_{c\mathbf{k},v\mathbf{k}}(-\mathbf{q})\right)^{*} W_{\mathbf{G}\mathbf{G}'}(\mathbf{q};\omega=0) M^{\mathbf{G}'}_{v'\mathbf{k}',c'\mathbf{k}'}(-\mathbf{q}), \quad \mathbf{q}=\mathbf{k}'-\mathbf{k} \tag{2.37}$$

Here, $M^{\mathbf{G}}_{n\mathbf{k},m\mathbf{k}'}(\mathbf{q}) = \langle \Psi_{n\mathbf{k}} | e^{-i(\mathbf{q}+\mathbf{G})\cdot\mathbf{r}} | \Psi_{m\mathbf{k}'} \rangle$ are plane-wave matrix elements between Bloch states, and $W_{\mathbf{G}\mathbf{G}'}(\mathbf{q};\omega=0)$ is the statically screened Coulomb interaction in reciprocal space.

In contrast, the exchange term (K^{x}) has its origin in the bare Coulomb potential $v_c(\mathbf{r}_1-\mathbf{r}_2)$ and is important to describe triplet-singlet excitonic splitting. In the case of optical absorption, which couples mainly to spin-singlet excitons in non-magnetic materials, this exchange term reads:

$$K^{\mathrm{x}}_{vc\mathbf{k},v'c'\mathbf{k}'} = 2\sum_{\mathbf{G}}\left(M^{\mathbf{G}}_{c\mathbf{k},c'\mathbf{k}'}(\mathbf{k}-\mathbf{k}')\right)^{*} v_c(\mathbf{k}-\mathbf{k}'+\mathbf{G}) M^{\mathbf{G}}_{v'\mathbf{k}',v\mathbf{k}}(\mathbf{k}-\mathbf{k}'), \tag{2.38}$$

where $v_c(\mathbf{Q})$ is the Fourier transform of the bare Coulomb potential [2].

2.9 Optical properties from the BSE

By solving the Bethe–Salpeter equation (BSE), one finds the excitonic energies Ω^λ and the relative exciton wavefunction coefficients $A^\lambda_{vc\mathbf{k}}$. They are used directly to build the imaginary part of the macroscopic dielectric function, $\mathrm{Im}[\epsilon_M(\omega)]$, which describes the material's optical absorption spectrum. Using Fermi's golden rule and linear response theory, the imaginary part of the macroscopic dielectric function for a light field incident with polarization vector $\mathbf{e}$ is given by:

$$\mathrm{Im}[\epsilon_M(\omega)] = \frac{4\pi^2 e^2}{\omega^2 \mathcal{V} m_0^2} \sum_\lambda \left| \sum_{vc\mathbf{k}} A^\lambda_{vc\mathbf{k}} \langle \psi_{c\mathbf{k}} | \mathbf{e} \cdot \hat{\mathbf{p}} | \psi_{v\mathbf{k}} \rangle \right|^2 \delta(\hbar\omega - \Omega^\lambda) \tag{2.39}$$

In this equation, e is the elementary charge, $\mathcal{V}$ is the volume of the unit cell (for periodic systems), m_0 is the free electron mass, and $\hat{\mathbf{p}}$ is the momentum operator. $\langle \psi_{c\mathbf{k}} | \mathbf{e} \cdot \hat{\mathbf{p}} | \psi_{v\mathbf{k}} \rangle$ is the momentum matrix element for the optical transition from a valence band state $\psi_{v\mathbf{k}}$ to a conduction band state $\psi_{c\mathbf{k}}$. The Dirac delta function, $\delta(\hbar\omega - \Omega^\lambda)$, guarantees energy conservation, i.e., absorption takes place if the photon energy $\hbar\omega$ matches some excitonic energy Ω^λ. In practice, the delta function in actual calculations is smeared out by a Lorentzian or Gaussian lineshape function [2, 23]. The summation over λ includes all of the excitonic states, and the inner summation over $v, c, \mathbf{k}$ with weighting using the exciton coefficients $A^\lambda_{vc\mathbf{k}}$ in a formal manner constructs the transition dipole moment of each exciton state. When the spin-orbit coupling (SOC) is large, the wavefunctions become two-component spinors $\psi_{v\mathbf{k}}$ and $\psi_{c\mathbf{k}}$, and the momentum operator $\hat{\mathbf{p}}$ has to be handled correctly to properly account for the selection rules and SOC-modified intensities. Correct calculation of these wavefunctions and quasiparticle energies in the presence of SOC is a key concern of this thesis.

3 Implementation

Building upon the theoretical background in Chapter 2, this chapter extends the second variation with local orbitals (SVLO) methodology to the Bethe–Salpeter equation (BSE) and describes its implementation in the all-electron full-potential (L)APW+lo package `exciting` [4]. The aim is to retain the accuracy of spin–orbit coupling (SOC) in the optical workflow while reducing the number of empty states required for convergence, consistent with the SVLO design [3] and the BSE implementation used for spectra [2].

3.1 Momentum matrix elements

The momentum matrix element $P^j_{nm}(\mathbf{k}) = \langle \Psi_{n\mathbf{k}} \,|\, \hat{p}_j \,|\, \Psi_{m\mathbf{k}} \rangle$ tells how strongly light polarized along direction j drives the transition $\Psi_{m\mathbf{k}} \to \Psi_{n\mathbf{k}}$. A larger $|P^j_{nm}(\mathbf{k})|$ yields a stronger contribution to the absorption for that polarization (see Chapter 2) [2]. We use $\hat{p}_j = -i\hbar\nabla_j$.

3.1.1 FV treatment

The first-variational (FV) treatment computes matrix elements between scalar-relativistic (SR) eigenstates $\Psi^{\mathrm{FV}}_{n\mathbf{k}}$. In this FV context, the state indices n, n' run from 1 to N_b^{SV}. These eigenstates are expanded in the (L)APW+lo basis, with $c^{\mathbf{G}}_{n\mathbf{k}}$ and $c^{\mu}_{n\mathbf{k}}$ being the expansion coefficients in the (L)APW $\phi^{(\mathrm{L})\mathrm{APW}}$ and local-orbital (LO) ϕ_μ subspaces, respectively. Expanded in the (L)APW+lo basis, the momentum matrix $P^j_{nn'\mathbf{k}}$ takes the block form:

$$\begin{aligned} P^j_{nn'\mathbf{k}} = &\sum_{\mathbf{G}\mathbf{G}'} (c^{\mathbf{G}}_{n\mathbf{k}})^* c^{\mathbf{G}'}_{n'\mathbf{k}} P^j_{\mathbf{G}\mathbf{G}'\mathbf{k}} + \sum_{\mathbf{G}\mu'} (c^{\mathbf{G}}_{n\mathbf{k}})^* c^{\mu'}_{n'\mathbf{k}} P^j_{\mathbf{G}\mu'\mathbf{k}} \\ &+ \sum_{\mu\mathbf{G}'} (c^{\mu}_{n\mathbf{k}})^* c^{\mathbf{G}'}_{n'\mathbf{k}} P^j_{\mu\mathbf{G}'\mathbf{k}} + \sum_{\mu\mu'} (c^{\mu}_{n\mathbf{k}})^* c^{\mu'}_{n'\mathbf{k}} P^j_{\mu\mu'\mathbf{k}}, \end{aligned} \tag{3.1}$$

constructed from block integrals between (L)APW $\phi^{(\mathrm{L})\mathrm{APW}}$ and LO ϕ_μ basis functions, evaluated via the muffin-tin/interstitial partition [4, 18]

$$\begin{aligned} P^j_{\mathbf{G}\mathbf{G}'\mathbf{k}} &= \big\langle \phi^{(\mathrm{L})\mathrm{APW}}_{\mathbf{G}+\mathbf{k}}(\mathbf{r}) \,\big|\, -i\hbar\nabla_j \,\big|\, \phi^{(\mathrm{L})\mathrm{APW}}_{\mathbf{G}'+\mathbf{k}}(\mathbf{r}) \big\rangle, \\ P^j_{\mathbf{G}\mu'\mathbf{k}} &= \big\langle \phi^{(\mathrm{L})\mathrm{APW}}_{\mathbf{G}+\mathbf{k}}(\mathbf{r}) \,\big|\, -i\hbar\nabla_j \,\big|\, \phi_{\mu'}(\mathbf{r}) \big\rangle, \\ P^j_{\mu\mathbf{G}'\mathbf{k}} &= \big\langle \phi_{\mu}(\mathbf{r}) \,\big|\, -i\hbar\nabla_j \,\big|\, \phi^{(\mathrm{L})\mathrm{APW}}_{\mathbf{G}'+\mathbf{k}}(\mathbf{r}) \big\rangle, \\ P^j_{\mu\mu'\mathbf{k}} &= \big\langle \phi_{\mu}(\mathbf{r}) \,\big|\, -i\hbar\nabla_j \,\big|\, \phi_{\mu'}(\mathbf{r}) \big\rangle. \end{aligned}$$

3.1.2 SV treatment

In the standard second-variational (SV) step [3], the SOC Hamiltonian is diagonalized within the basis of SR eigenstates $\Psi^{\mathrm{FV}}_{n\mathbf{k}\sigma}$, where the basis indices n, n' run from 1 to N_b^{SV}. This yields SV transformation coefficients $C^{\mathrm{SV}}_{an\sigma\mathbf{k}}$. Since the momentum operator $\hat{p}_j$ is spin-diagonal, the matrix element $P^{j,\mathrm{SV}}_{ab}(\mathbf{k})$ between the resulting spinor states a and b is obtained by rotating the FV matrix $P^{j}_{nn'\mathbf{k}}$:

$$P^{j,\mathrm{SV}}_{ab}(\mathbf{k}) = \sum_{\sigma} \sum_{n,n'=1}^{N_b^{\mathrm{SV}}} \left(C^{\mathrm{SV}}_{an\sigma\mathbf{k}}\right)^{*} P^{j}_{nn'\mathbf{k}}\, C^{\mathrm{SV}}_{bn'\sigma\mathbf{k}}. \tag{3.2}$$

This transformation incorporates the SOC effects captured by the SV diagonalization [3, 18].

3.1.3 SVLO treatment

The SVLO method uses an enhanced basis for the standard second variation [3], constructed as follows:

- **Modification of FV functions:** LO components are removed from SR eigenstates $\Psi^{\mathrm{FV}}_{j\mathbf{k}\sigma}$ to yield modified functions $\overline{\Psi}^{\mathrm{FV}}_{j\mathbf{k}\sigma}$ [3]:

$$\overline{\Psi}^{\mathrm{FV}}_{j\mathbf{k}\sigma}(\mathbf{r}) = \sum_{\mathbf{G}} C_{\mathbf{k}\sigma\mathbf{G}j}\, \phi_{\mathbf{G}+\mathbf{k}}(\mathbf{r}). \tag{3.3}$$

- **Explicit inclusion of LOs:** Original LOs $\{\phi_\mu\}$ are added explicitly to the basis alongside $\overline{\Psi}^{\mathrm{FV}}_{n\mathbf{k}}$ [3].

This combined basis $\{\overline{\Psi}^{\mathrm{FV}}\} \cup \{\phi_\mu\}$ is non-orthogonal. Diagonalizing the SOC Hamiltonian requires solving a generalized eigenvalue problem involving the overlap matrix S^{SVLO} [3, 24, 25, 26, 27]. This yields SVLO coefficients $C^{\mathrm{SVLO}}_{an\sigma\mathbf{k}}$. The momentum operator $P^{j}_{nn'\mathbf{k}}$ is represented in this extended basis using a new unified index n. In this SVLO context, the unified index n (and n') spans from 1 to $N_b^{\mathrm{SVLO}} = N_b^{\mathrm{SV}} + N_{\mathrm{LO}}$. The indices $\{1, \ldots, N_b^{\mathrm{SV}}\}$ refer to the modified FV functions $\overline{\Psi}^{\mathrm{FV}}$, while the indices $\{N_b^{\mathrm{SV}}{+}1, \ldots, N_b^{\mathrm{SV}}{+}N_{\mathrm{LO}}\}$ (also denoted by μ, μ') refer to the LO functions ϕ_μ. This representation results in a block structure: We define the re-orthogonalized FV block $\bar{P}^{j}_{nn'\mathbf{k}}$ as:

$$\bar{P}^{j}_{nn'\mathbf{k}} = \begin{cases} \displaystyle\sum_{\mathbf{G}\mathbf{G}'} \left(c^{\mathbf{G}}_{n\mathbf{k}}\right)^{*} c^{\mathbf{G}'}_{n'\mathbf{k}}\, P^{j}_{\mathbf{G}\mathbf{G}'\mathbf{k}}, & \text{if } 1 \le (n,n') \le N_b^{\mathrm{SV}}, \\ \displaystyle\sum_{\mathbf{G}\mu'} \left(c^{\mathbf{G}}_{n\mathbf{k}}\right)^{*} c^{\mu'}_{n'\mathbf{k}}\, P^{j}_{\mathbf{G}\mu'\mathbf{k}}, & \text{if } 1 \le n \le N_b^{\mathrm{SV}},\ N_b^{\mathrm{SV}}{+}1 \le n' \le N_b^{\mathrm{SV}}{+}N_{\mathrm{LO}}, \\ \displaystyle\sum_{\mu\mathbf{G}'} \left(c^{\mu}_{n\mathbf{k}}\right)^{*} c^{\mathbf{G}'}_{n'\mathbf{k}}\, P^{j}_{\mu\mathbf{G}'\mathbf{k}}, & \text{if } N_b^{\mathrm{SV}}{+}1 \le n \le N_b^{\mathrm{SV}}{+}N_{\mathrm{LO}},\ 1 \le n' \le N_b^{\mathrm{SV}}, \\ \displaystyle\sum_{\mu\mu'} \left(c^{\mu}_{n\mathbf{k}}\right)^{*} c^{\mu'}_{n'\mathbf{k}}\, P^{j}_{\mu\mu'\mathbf{k}}, & \text{if } N_b^{\mathrm{SV}}{+}1 \le (n,n') \le N_b^{\mathrm{SV}}{+}N_{\mathrm{LO}}. \end{cases} \tag{3.4}$$

Here, $\overline{P}^{j}_{nn'\mathbf{k}}$ represents the FV block re-orthogonalized for the SVLO basis [27]. Hermiticity implies $P^{j}_{\mu n'\mathbf{k}} = (P^{j}_{n'\mu\mathbf{k}})^{*}$. Since $\hat{p}_j$ is spin-diagonal, the final spinor element $P^{j,\mathrm{SVLO}}_{ab}(\mathbf{k})$ is obtained by applying the SVLO transformation:

$$P^{j,\mathrm{SVLO}}_{ab}(\mathbf{k}) = \sum_{\sigma} \sum_{n=1}^{N_b^{\mathrm{SVLO}}} \sum_{n'=1}^{N_b^{\mathrm{SVLO}}} \left(C^{\mathrm{SVLO}}_{an\sigma\mathbf{k}}\right)^{*} \bar{P}^{j}_{nn'\mathbf{k}}\, C^{\mathrm{SVLO}}_{bn'\sigma\mathbf{k}}. \tag{3.5}$$

This follows the SVLO strategy of Ref. [3].

3.2 Plane-wave matrix elements

The plane wave operator $\hat{\rho}_{\mathbf{q}+\mathbf{G}} = e^{-i(\mathbf{q}+\mathbf{G})\cdot\mathbf{r}}$ indicates the Fourier components of the transition density between Bloch states. Its matrix element

$$M^{\mathbf{G}}_{n\mathbf{k},m\mathbf{k}'}(\mathbf{q}) = \langle \Psi_{n\mathbf{k}} \,|\, e^{-i(\mathbf{q}+\mathbf{G})\cdot\mathbf{r}} \,|\, \Psi_{m\mathbf{k}'} \rangle, \qquad \mathbf{q} = \mathbf{k}' - \mathbf{k},$$

is the $(\mathbf{q}+\mathbf{G})$-component of the transition density function between the electron and hole. The set M constitutes both the attractive screening-direct term and the repulsive exchange term of the BSE kernel, while the $\mathbf{G} \neq 0$ component encodes localised field effects significant in low-dimensional or anisotropic systems [2, 19, 20].

3.2.1 FV treatment

The FV plane-wave matrix element $M^{\mathbf{G}}_{n\mathbf{k},m\mathbf{k}'}(\mathbf{q})$ is computed between scalar-relativistic (SR) eigenstates $\Psi_{n\mathbf{k}}$ and $\Psi_{m\mathbf{k}'}$. In this context, the state indices n, m run from 1 to N_b^{SV}. These states are expanded using coefficients, $c^{\mathbf{G}_1}_{n\mathbf{k}}$, $c^{\mu_2}_{m\mathbf{k}'}$) in the (L)APW and LO subspaces. The matrix element decomposes into (L)APW+lo blocks:

$$\begin{aligned} M^{\mathbf{G}}_{n\mathbf{k},m\mathbf{k}'}(\mathbf{q}) = &\sum_{\mathbf{G}_1\mathbf{G}_2} (c^{\mathbf{G}_1}_{n\mathbf{k}})^{*} c^{\mathbf{G}_2}_{m\mathbf{k}'}\, M^{\mathbf{G}}_{\mathbf{G}_1\mathbf{G}_2}(\mathbf{k},\mathbf{k}',\mathbf{q}) \\ &+ \sum_{\mathbf{G}_1\mu_2} (c^{\mathbf{G}_1}_{n\mathbf{k}})^{*} c^{\mu_2}_{m\mathbf{k}'}\, M^{\mathbf{G}}_{\mathbf{G}_1\mu_2}(\mathbf{k},\mathbf{k}',\mathbf{q}) \\ &+ \sum_{\mu_1\mathbf{G}_2} (c^{\mu_1}_{n\mathbf{k}})^{*} c^{\mathbf{G}_2}_{m\mathbf{k}'}\, M^{\mathbf{G}}_{\mu_1\mathbf{G}_2}(\mathbf{k},\mathbf{k}',\mathbf{q}) \\ &+ \sum_{\mu_1\mu_2} (c^{\mu_1}_{n\mathbf{k}})^{*} c^{\mu_2}_{m\mathbf{k}'}\, M^{\mathbf{G}}_{\mu_1\mu_2}(\mathbf{k},\mathbf{k}',\mathbf{q}). \end{aligned} \tag{3.6}$$

Here each block is a standard LAPW+lo integral of $e^{-i(\mathbf{q}+\mathbf{G})\cdot\mathbf{r}}$ evaluated with the muffin-tin/interstitial partition, fully analogous to the momentum case [4]:

$$
\begin{aligned}
M^{\mathbf{G}}_{\mathbf{G}_1\mathbf{G}_2}(\mathbf{k},\mathbf{k}',\mathbf{q}) &= \left\langle \phi^{(\mathrm{L})\mathrm{APW}}_{\mathbf{G}_1+\mathbf{k}} \,\middle|\, e^{-i(\mathbf{q}+\mathbf{G})\cdot\mathbf{r}} \,\middle|\, \phi^{(\mathrm{L})\mathrm{APW}}_{\mathbf{G}_2+\mathbf{k}'} \right\rangle, \\
M^{\mathbf{G}}_{\mathbf{G}_1\mu_2}(\mathbf{k},\mathbf{k}',\mathbf{q}) &= \left\langle \phi^{(\mathrm{L})\mathrm{APW}}_{\mathbf{G}_1+\mathbf{k}} \,\middle|\, e^{-i(\mathbf{q}+\mathbf{G})\cdot\mathbf{r}} \,\middle|\, \phi_{\mu_2} \right\rangle, \\
M^{\mathbf{G}}_{\mu_1\mathbf{G}_2}(\mathbf{k},\mathbf{k}',\mathbf{q}) &= \left\langle \phi_{\mu_1} \,\middle|\, e^{-i(\mathbf{q}+\mathbf{G})\cdot\mathbf{r}} \,\middle|\, \phi^{(\mathrm{L})\mathrm{APW}}_{\mathbf{G}_2+\mathbf{k}'} \right\rangle, \\
M^{\mathbf{G}}_{\mu_1\mu_2}(\mathbf{k},\mathbf{k}',\mathbf{q}) &= \left\langle \phi_{\mu_1} \,\middle|\, e^{-i(\mathbf{q}+\mathbf{G})\cdot\mathbf{r}} \,\middle|\, \phi_{\mu_2} \right\rangle.
\end{aligned}
$$

3.2.2 SV treatment

The plane-wave operator $e^{-i(\mathbf{q}+\mathbf{G})\cdot\mathbf{r}}$ is spin-diagonal. The matrix element is computed within the basis of SR eigenstates $\Psi^{\mathrm{FV}}_{n\mathbf{k}\sigma}$, where the basis indices n, n' run from 1 to N_b^{SV}. Thus, the matrix element $M^{\mathbf{G},\mathrm{SV}}_{ab\,\mathbf{k}\mathbf{k}'}(\mathbf{q})$ in the SV spinor basis is obtained by rotating the FV matrix $M^{\mathbf{G}}_{n\mathbf{k},n'\mathbf{k}'}(\mathbf{q})$ using the SV coefficients $C^{\mathrm{SV}}_{an\sigma\mathbf{k}}$:

$$
M^{\mathbf{G},\mathrm{SV}}_{ab\,\mathbf{k}\mathbf{k}'}(\mathbf{q}) = \sum_{\sigma} \sum_{n,n'=1}^{N_b^{\mathrm{SV}}} \left(C^{\mathrm{SV}}_{an\sigma\mathbf{k}}\right)^* M^{\mathbf{G}}_{n\mathbf{k},n'\mathbf{k}'}(\mathbf{q})\, C^{\mathrm{SV}}_{bn'\sigma\mathbf{k}'}. \tag{3.7}
$$

3.2.3 SVLO treatment

Analogous to the momentum operator section, $M^{\mathbf{G}}$ is represented in the extended, non-orthogonal SVLO basis. This basis uses a new unified index n (and n') spanning from 1 to $N_b^{\mathrm{SVLO}} = N_b^{\mathrm{SV}} + N_{\mathrm{LO}}$. The indices $\{1,\ldots,N_b^{\mathrm{SV}}\}$ refer to the modified FV functions $\overline{\Psi}^{\mathrm{FV}}$, while the indices $\{N_b^{\mathrm{SV}}{+}1,\ldots,N_b^{\mathrm{SV}}{+}N_{\mathrm{LO}}\}$ refer to the LO functions ϕ_μ. This yields the block matrix $M^{\mathbf{G}}_{nn'}(\mathbf{k},\mathbf{k}';\mathbf{q})$. The final SVLO matrix element $M^{\mathbf{G},\mathrm{SVLO}}_{ab\,\mathbf{k}\mathbf{k}'}(\mathbf{q})$ between spinor states a and b is obtained by applying the SVLO transformation $C^{\mathrm{SVLO}}_{an\sigma\mathbf{k}}$:

$$
M^{\mathbf{G},\mathrm{SVLO}}_{ab\,\mathbf{k}\mathbf{k}'}(\mathbf{q}) = \sum_{\sigma} \sum_{n=1}^{N_b^{\mathrm{SVLO}}} \sum_{n'=1}^{N_b^{\mathrm{SVLO}}} \left(C^{\mathrm{SVLO}}_{an\sigma\mathbf{k}}\right)^* bar M^{\mathbf{G}}_{nn'}(\mathbf{k},\mathbf{k}';\mathbf{q})\, C^{\mathrm{SVLO}}_{bn'\sigma\mathbf{k}'}, \tag{3.8}
$$

with the blocks $M^{\mathbf{G}}_{nn'}(\mathbf{k},\mathbf{k}';\mathbf{q})$ defined by:

$$
\bar{M}^{\mathbf{G}}_{nn'}(\mathbf{k},\mathbf{k}';\mathbf{q}) = \begin{cases}
\displaystyle\sum_{\mathbf{G}_1\mathbf{G}_2} \left(c^{\mathbf{G}_1}_{n\mathbf{k}}\right)^* c^{\mathbf{G}_2}_{n'\mathbf{k}'}\, M^{\mathbf{G}}_{\mathbf{G}_1\mathbf{G}_2}(\mathbf{k},\mathbf{k}';\mathbf{q}), & \text{if } 1 \le (n,n') \le N_b^{\mathrm{SV}}, \\
\displaystyle\sum_{\mathbf{G}_1\mu_2} \left(c^{\mathbf{G}_1}_{n\mathbf{k}}\right)^* c^{\mu_2}_{n'\mathbf{k}'}\, M^{\mathbf{G}}_{\mathbf{G}_1\mu_2}(\mathbf{k},\mathbf{k}';\mathbf{q}), & \text{if } 1 \le n \le N_b^{\mathrm{SV}},\ N_b^{\mathrm{SV}}{+}1 \le n' \le N_b^{\mathrm{SV}}{+}N_{\mathrm{LO}}, \\
\displaystyle\sum_{\mu_1\mathbf{G}_2} \left(c^{\mu_1}_{n\mathbf{k}}\right)^* c^{\mathbf{G}_2}_{n'\mathbf{k}'}\, M^{\mathbf{G}}_{\mu_1\mathbf{G}_2}(\mathbf{k},\mathbf{k}';\mathbf{q}), & \text{if } N_b^{\mathrm{SV}}{+}1 \le n \le N_b^{\mathrm{SV}}{+}N_{\mathrm{LO}},\ 1 \le n' \le N_b^{\mathrm{SV}}, \\
\displaystyle\sum_{\mu_1\mu_2} \left(c^{\mu_1}_{n\mathbf{k}}\right)^* c^{\mu_2}_{n'\mathbf{k}'}\, M^{\mathbf{G}}_{\mu_1\mu_2}(\mathbf{k},\mathbf{k}';\mathbf{q}), & \text{if } N_b^{\mathrm{SV}}{+}1 \le (n,n') \le N_b^{\mathrm{SV}}{+}N_{\mathrm{LO}}.
\end{cases} \tag{3.9}
$$

Here, $\overline{M}^{\mathbf{G}}_{nn'}$ denotes the FV block after Löwdin symmetric orthogonalization to the SVLO basis [27]. The property $M^{\mathbf{G}}_{nn'}(\mathbf{k},\mathbf{k}';\mathbf{q}) = \left(M^{\mathbf{G}}_{n'n}(\mathbf{k}',\mathbf{k};-\mathbf{q})\right)^*$ ensures a Hermitian static BSE kernel [2].

3.3 Assembly of the interaction kernel and effective Hamiltonian

3.3.1 Use of momentum matrix elements

The polarization-resolved momentum elements $P^j_{cv}(\mathbf{k})$ weight how strongly each interband pair $(v,c,\mathbf{k})$ couples to light polarized along j. For each exciton λ we form the dipole amplitude

$$D^j_\lambda = \sum_{vc\mathbf{k}} A^\lambda_{vc\mathbf{k}} \frac{P^j_{cv}(\mathbf{k})}{E^{\mathrm{QP}}_{c\mathbf{k}} - E^{\mathrm{QP}}_{v\mathbf{k}}}, \tag{3.10}$$

which sets the polarization dependence of the absorption used in the Eq. (2.39) [2, 22].

3.3.2 Use of plane-wave matrix elements

The plane-wave elements $M^{\mathbf{G}}_{n\mathbf{k},m\mathbf{k}'}(\mathbf{q})$ are the essential building blocks of the electron-hole kernel. We assemble the static hermitian kernel as in Eqs. (2.37) and (2.38), using $\mathbf{q} = \mathbf{k}' - \mathbf{k}$ and $W_{\mathbf{G}\mathbf{G}'}(\mathbf{q};0)$ from Eq. (2.31). The static choice $W(\omega{=}0)$ is standard for near-edge spectra [2, 19, 20, 22]. We then assemble and diagonalize only the resonant block of the Bethe-Salpeter operator (Eq. (2.32)), obtaining Ω^λ and $A^\lambda_{vc\mathbf{k}}$; from these we form D^j_λ via Eq. (3.10) and calculate the absorption with Eq. (2.39).

4 Results

In order to successfully demonstrate implementation and validation of the performance of the SVLO-BSE method, comprehensive tests were conducted on four representative materials with spin-orbit coupling effects : MoS_2, PbI_2, $CsPbI_3$, and Cs_2PbI_4. As an application case study, we then apply the SVLO-based workflow to the halide compound $Cs_4AgBiBr_8$, modeled here as a periodic slab. Taken together, these cases provide a coherent testbed for evaluating and illustrating the method.

4.1 SVLO-BSE Implementation Verification Criteria

In order to verify the implementation and validation of the SVLO-BSE approach, test calculations were carried out on four representative materials with spin-orbit coupling effects. In addition, we include an SVLO application case. These materials form a good basis for the verification of the method. The evaluation of SVLO-BSE implementation is carried out based on three basic criteria in order to verify the SVLO-BSE method implementation:

Reproducibility: The implementation must precisely reproduce the results from the SV-BSE approach. This test decides whether the SVLO extension reproduces physical accuracy of the BSE method without sacrificing convergence and comparable results regarding basis set sizes.

Efficiency: A key advantage of the SVLO approach is that it has the ability to converge with significantly fewer empty states than the standard SV method. This numerical advantage can be quantified by comparing the number of basis sets that need to converge in standard SV and SVLO. For materials with large SOC, the SVLO approach will probably require significantly smaller basis set sizes.

Accuracy: The method must accurately capture the underlying physics of spin-orbit coupling effects on optical spectra such as Dirac-type local orbitals in Section 2.6. This is verified by comparing results at various levels of approximation along the BSE and preserving the relative significance of various interaction terms appropriately.

4.2 Computational Details

All calculations were performed using the all-electron full-potential linearized augmented plane wave plus local orbitals (LAPW+lo) method as implemented in the `exciting` code [4]. Four

representative materials were selected for the validation study: MoS_2 as a prototypical two-dimensional transition metal dichalcogenide with moderate SOC, PbI_2 and $CsPbI_3$ as materials exhibiting strong spin-orbit coupling due to heavy Pb atoms, and Cs_2PbI_4 as a two-dimensional halide perovskite. For Cs_2PbI_4, the organic cations typically found in hybrid perovskites were replaced with Cs for computational convenience while maintaining the essential physics of the system [28].

As a separate application case, $Cs_4AgBiBr_8$ was modeled and computed using the same DFT→SVLO→BSE workflow in `exciting`. We adopted the PBE-optimized crystal structure from [29] (see also [30] for the series), and used the computational settings listed in Table 4.1.

4.2.1 Ground State Calculations

Experimentally determined lattice constants and atomic positions were employed for MoS_2, PbI_2, and $CsPbI_3$ [3], whereas for Cs_2PbI_4 and $Cs_4AgBiBr_8$ we used literature DFT-relaxed structures [28, 29]. The exchange-correlation effects were treated within the generalized gradient approximation (GGA), using the Perdew–Burke–Ernzerhof (PBE) functional [10] for MoS_2, PbI_2, $CsPbI_3$, and $Cs_4AgBiBr_8$, while the PBEsol functional was utilized for Cs_2PbI_4 to better account for the lattice properties of this perovskite structure. The computational parameters for ground-state calculations were carefully converged to ensure accuracy. The k-point meshes for Brillouin-zone sampling were chosen as $6\times6\times1$ for MoS_2 (reflecting its quasi-2D nature), $6\times6\times4$ for PbI_2, $3\times3\times2$ for $CsPbI_3$, $7\times7\times7$ for Cs_2PbI_4, and $6\times6\times1$ for $Cs_4AgBiBr_8$. The dimensionless LAPW cutoff parameter $R_{\mathrm{MT}}^{\mathrm{min}}\times G_{\mathrm{max}}$ (rgkmax) was set to 8.0 for MoS_2 and PbI_2, 9.0 for $CsPbI_3$, 12.0 for Cs_2PbI_4, and 7.5 for $Cs_4AgBiBr_8$. These parameters were determined by imposing a convergence criterion of 10 meV for the band-gap energy.

Table 4.1: Summary of computational parameters used in ground-state calculations.

Parameter	**MoS_2**	**PbI_2**	**$CsPbI_3$**	**Cs_2PbI_4**	**$Cs_4AgBiBr_8$**
k-mesh	$6\times6\times1$	$6\times6\times4$	$3\times3\times2$	$7\times7\times7$	$6\times6\times1$
rgkmax	8.0	8.0	9.0	12.0	7.5
XC functional	PBE	PBE	PBE	PBEsol	PBE

The number of local orbitals and occupied states required for convergence in the SVLO calculations varied significantly between materials, reflecting their different electronic structures and SOC strengths. These values are summarized in Table 4.2. Unless noted otherwise, ground-state settings follow Ref. [3]; for Cs_2PbI_4 we adopt the setup of Ref. [28], and for $Cs_4AgBiBr_8$ they were established by our own convergence tests based on the PBE-relaxed structure of Ref. [29].

Table 4.2: Number of local orbitals and occupied states used in SVLO calculations. For PbI_2, $CsPbI_3$ and $Cs_4AgBiBr_8$, rows labeled "$p_{1/2}$ LOs" indicate runs where additional $p_{1/2}$-type local orbitals were added.

Material	N_{LO}	N_{occ}
MoS_2	35	13
PbI_2	73	33
PbI_2 ($p_{1/2}$ LOs)	109	33
$CsPbI_3$	496	228
$CsPbI_3$ ($p_{1/2}$ LOs)	736	228
Cs_2PbI_4	126	60
$Cs_4AgBiBr_8$	766	174
$Cs_4AgBiBr_8$ ($p_{1/2}$ LOs)	844	174

4.2.2 Excited State Calculations

For the BSE calculations, the k-point meshes were chosen to balance accuracy and computational cost, and the plane-wave cutoff for the screened Coulomb interaction was tuned per material. The parameters used to compute the spectra are listed in Table 4.3.

Table 4.3: BSE calculation parameters for optical spectra.

Parameter	**MoS_2**	**PbI_2**	**$CsPbI_3$**	**Cs_2PbI_4**	**$Cs_4AgBiBr_8$**
`k-mesh (BSE)`	6×6×1	3×3×2	3×3×2	3×3×3	6×6×1
`gqmax`	1.5	2.8	1.0	1.5	1.5

To check convergence, we varied two empty-state cutoffs: $\langle xs \rangle$ *nempty* for the number of empty states used to build the BSE Hamiltonian, and $\langle screen \rangle$ *nempty* for the number used in the dielectric screening W. Both were increased until the first exciton energy satisfied a strict convergence criterion of $10\ \mathrm{meV}$ [3].

4.3 Optical Spectra

The optical absorption spectra were obtained by solving the Bethe–Salpeter equation (Eq. (2.32)) and calculating the imaginary part of the macroscopic dielectric function according to Eq. (2.39). The spectra are determined by the combination of momentum matrix elements $\langle \psi_{c\mathbf{k}} | \mathbf{e} \cdot \hat{\mathbf{p}} | \psi_{v\mathbf{k}} \rangle$ and excitonic coefficients $A^{\lambda}_{vc\mathbf{k}}$.

4.4 Exciton Energy

The exciton binding energy E_b is defined as the difference between the band gap and the lowest excitonic transition energy :

$$E_b = E_{\text{gap}} - E_1 \tag{4.1}$$

where E_{gap} represents the minimum direct gap from the band structure and E_1 is the energy of the lowest exciton obtained from solving the BSE.

The convergence behavior of the exciton energy was analyzed by examining E_1 as a function of both $\langle xs \rangle$ *nempty* and $\langle screen \rangle$ *nempty*. As discussed in Section 2.8, $\langle xs \rangle$ *nempty* determines the size of the electron–hole pair basis used to construct the BSE Hamiltonian, directly affecting the diagonal terms $(E_{c\mathbf{k}} - E_{v\mathbf{k}})$. Meanwhile, $\langle screen \rangle$ *nempty* controls the quality of the screened Coulomb interaction W entering the direct interaction kernel K^{dir}, which is crucial for accurately capturing the excitonic binding.

4.5 MoS_2

Molybdenum disulfide (MoS_2) is used as a test system to validate the SVLO-BSE implementation. MoS_2 is a prototype transition metal dichalcogenide and exhibits pronounced spin-orbit coupling effects. In the monolayer limit, MoS_2 has a direct optical gap at the K point. This is the case considered here and is especially relevant for optoelectronic applications. The coupling of spin and orbital momentum in MoS_2 causes the splitting of the valence band at the K point, described by a spin-orbit splitting of about 150 meV, which essentially determines its optical properties through the distinct excitonic peaks [31].

Figure 4.1 demonstrates the very good agreement between the SVLO and SV methods for all levels of approximation in MoS_2. Panels (a) and (b) present the singlet exciton spectra; the first bright exciton appears at about 0.95 eV for both in-plane and out-of-plane polarization, and the two methods overlap essentially perfectly. Panels (c) and (d) show the RPA spectra and panels (e) and (f) the IP spectra; both exhibit an absorption onset near 1.70 eV. The exciton binding energy, which is calculated by subtracting the energy of the first exciton 0.95 eV from the band gap 1.70 eV, is 0.75 eV. Such a large binding energy is typical for two-dimensional semiconductors, in which decreased dielectric screening increases the Coulombic interaction between holes and electrons. The robust excitonic features in MoS_2 point to the significance of many-body interactions in governing the optical properties of two-dimensional systems. The anisotropies between in-plane and out-of-plane polarized spectra are due to the inherent anisotropic character of layered materials. In MoS_2, strong in-plane Mo–S covalent bonding and weak out-of-plane coupling make the structure anisotropic, which, together with the in-plane character of the band-edge states—results in a markedly stronger in-plane optical response [32, 33]. The valence band maximum is dominated by Mo $d_{x^2-y^2}$ and d_{xy} orbitals with strong in-plane character, while out-of-plane polarized light couples less efficiently due to

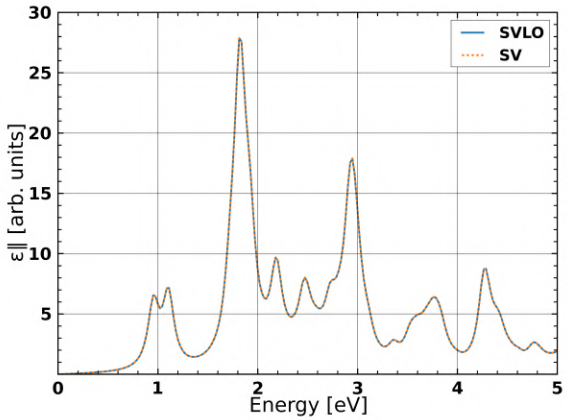

(a) In-plane singlet spectra: SVLO vs SV

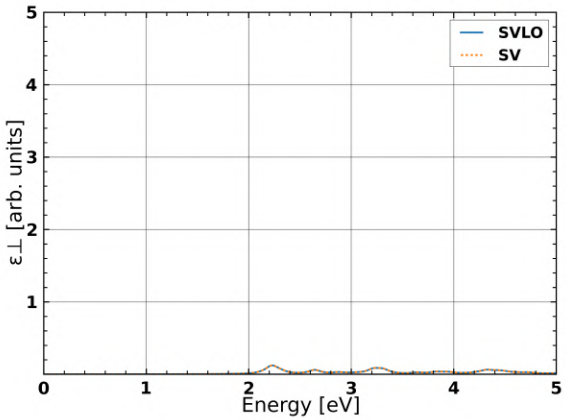

(b) Out-of-plane singlet spectra: SVLO vs SV

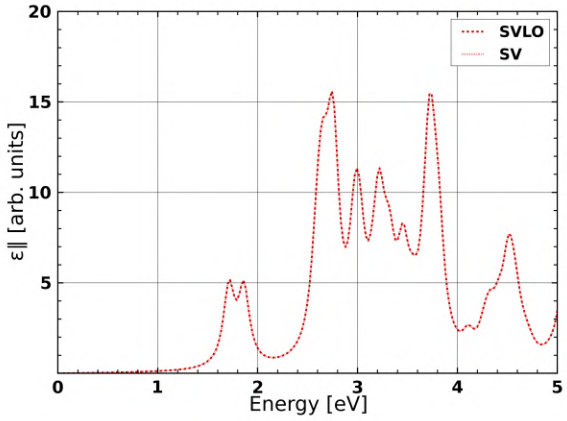

(c) In-plane RPA spectra: SVLO vs SV

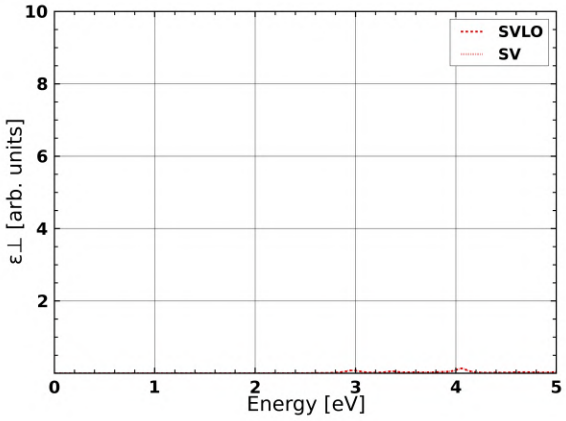

(d) Out-of-plane RPA spectra: SVLO vs SV

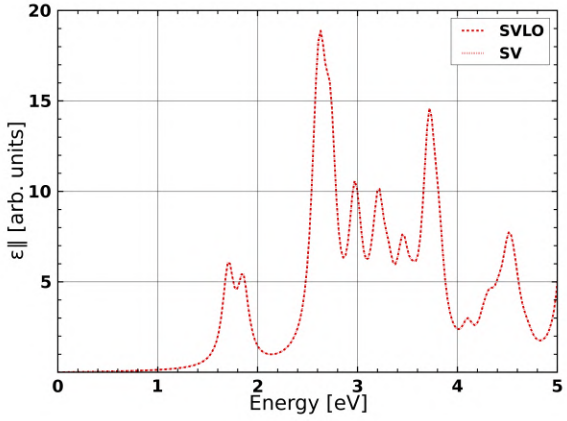

(e) In-plane IP spectra: SVLO vs SV

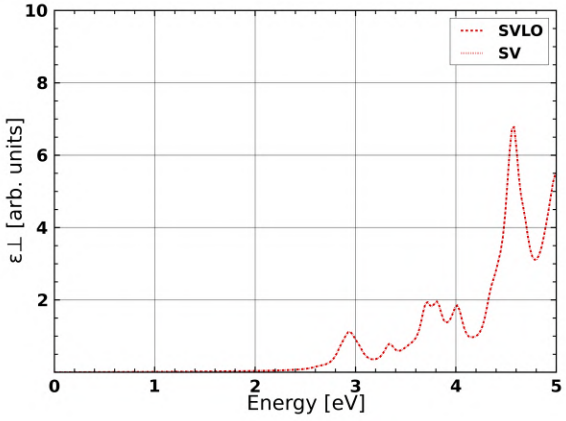

(f) Out-of-plane IP spectra: SVLO vs SV

Figure 4.1: Optical absorption spectra of MoS_2 comparing SVLO and SV methods. (a,b) Singlet BSE; (c,d) RPA; (e,f) IP.

unfavorable orbital overlap [34, 35, 36]. The structural anisotropy here, when coupled with quantum confinement effects in the out-of-plane direction, results in polarization-dependent oscillator strengths and peak intensities [32, 37, 38].

The exchange kernel within the BSE is important in redistributing oscillator strength among polarization channels. While the Independent Particle treatment deals with the transitions separately, both the RPA and singlet calculations incorporate the exchange interactions that couple different polarization directions via off-diagonal matrix elements [20]. These exchange couplings cause local-field effects that change relative peak positions and intensities in different polarization directions. The RPA includes screening effects through the response function but still treats electron-hole pairs as uncorrelated, while the complete treatment of BSE treats bound exciton states and their polarization-dependent characteristics through the complete interaction kernel [2, 19, 21].

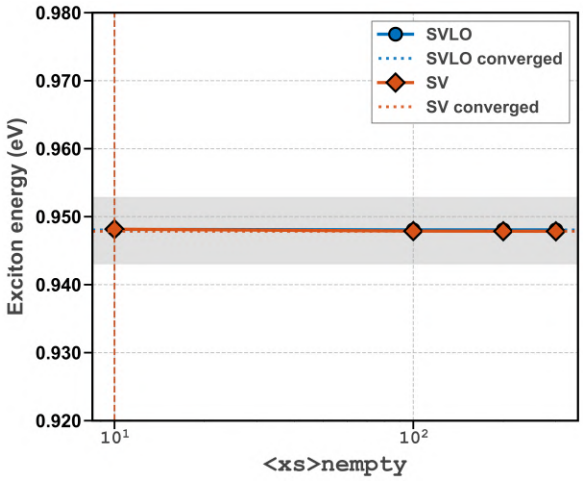

(a) Singlet: first exciton energy vs $\langle xs \rangle$ *nempty*

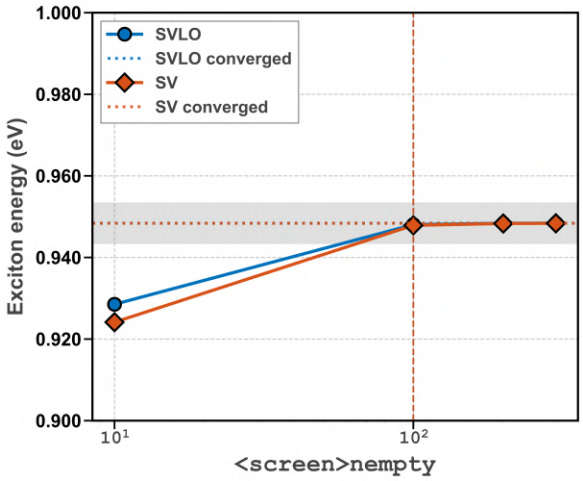

(b) Singlet: first exciton energy vs $\langle screen \rangle$ *nempty*

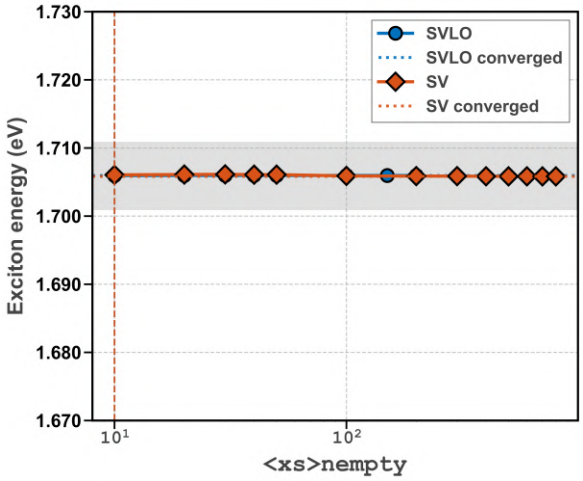

(c) IP: first exciton energy vs $\langle xs \rangle$ *nempty*

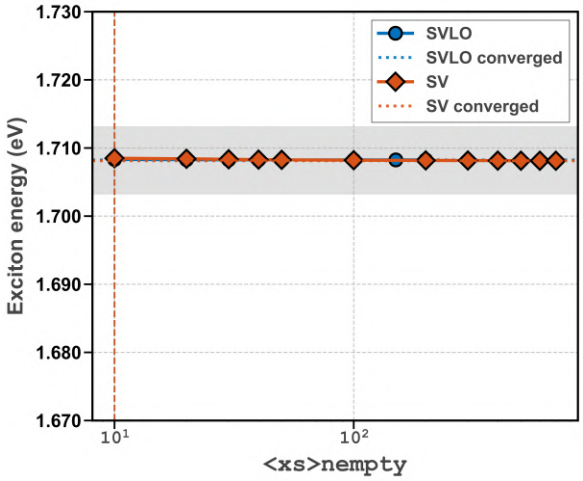

(d) RPA: first exciton energy vs $\langle xs \rangle$ *nempty*

Figure 4.2: Convergence summary for MoS_2 (SVLO vs SV). (a,b) Singlet BSE vs $\langle xs \rangle$ *nempty*, $\langle screen \rangle$ *nempty*; (c,d) IP/RPA vs $\langle xs \rangle$ *nempty*.

Figure 4.2 shows that, for MoS_2, the singlet first exciton energy converges near 0.95 eV at essentially the same $\langle xs \rangle$ $nempty$ and $\langle screen \rangle$ $nempty$ for SVLO and SV, while IP/RPA peak near 1.70 eV. Because the SOC in MoS_2 is only moderate, SVLO does not give a practical advantage here: spectra and convergence behaviour are effectively identical to SV.

4.6 PbI_2

PbI_2 is an excellent example to test the SVLO-BSE implementation and to investigate systems with strong spin-orbit coupling. This layered semiconductor compound consists of heavy lead atoms and contains strong spin-orbit coupling effects that strongly impact its electronic and optical properties. The compound possesses a direct band gap in the visible range and is used for a precursor of halide perovskites, making it highly useful for optoelectronics device applications [1, 3].

The effect of SOC on the electronic structure of PbI_2 is significant. Ground-state calculations show that the band gap decreases drastically from 2.20 eV in the scalar-relativistic treatment to 1.40 eV when Dirac-type $p_{1/2}$ local orbitals are considered. This significant reduction of the band gap requires proper SOC treatment for this material. In the SVLO setups used here, we employ $N_{\mathrm{LO}} = 73$ for SVLO(p) and $N_{\mathrm{LO}} = 109$ for SVLO($p_{1/2}$).

Figure 4.3 compares the optical absorption spectra obtained from various approximation levels. The first excitonic peak at 1.23 eV occurs for both in-plane and out-of-plane polarizations, as the spectra are in excellent agreement between SVLO and SV methods. Figure 4.4 shows that including Dirac-type $p_{1/2}$ local orbitals [SVLO($p_{1/2}$)] produces a pronounced redshift of the first excitonic peak from $1.23\ \mathrm{eV}$ to $1.01\ \mathrm{eV}$, consistent with the further SVLO-driven gap reduction [3]. With $E_g = 1.40\ \mathrm{eV}$, this corresponds to an exciton binding energy $E_b \approx 0.39\ \mathrm{eV}$ for SVLO($p_{1/2}$). The IP approximation places the absorption edge at 1.66 eV, corresponding to the band gap. The RPA calculation, including exchange interactions, maintains the first peak at 1.66 eV with modified oscillator strengths. The full singlet calculation reveals a significant redshift to 1.23 eV, yielding an exciton binding energy of 0.43 eV. This binding energy is characteristic of layered semiconductors, where reduced dielectric screening in the out-of-plane direction enhances the electron-hole attraction. The manner in which the convergence is approached with respect to the number of empty states is a strong indication of the success of the SVLO method. As apparent in Figure 4.5, the SVLO method achieves adequately converged spectra with as little as 50 empty states included in the $\langle xs \rangle$ $nempty$ block. Notably, the convergence is especially quick for the leading excitonic peak at 1.23 eV, which is stable even when considering only 10 empty states. Features at higher energies have a comparatively slower convergence behavior. However, all spectral features are completely converged at 50 states. By way of comparison, the standard SV approach shows much slower convergence behavior, requiring a considerably larger basis set size. With 10 empty states, the position of the first peak in the SV calculation is incorrect at about 1.20 eV, which corrects slowly toward the actual value of 1.23 eV as higher states are included. Despite the availability of 300 unoccupied states, the SV spectra exhibit large variations, especially in relative peak intensities above 2 eV. Full convergence of the SV approach takes approximately 400 unoccupied states.

The exciton energy convergence study, shown in Figure 4.6, is a further proof of this increased efficiency. In calculations for singlet excitons, the SVLO method reaches its converged value of

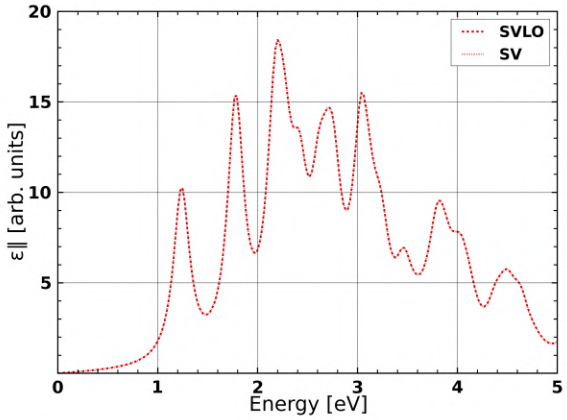

(a) In-plane singlet spectra: SVLO vs SV

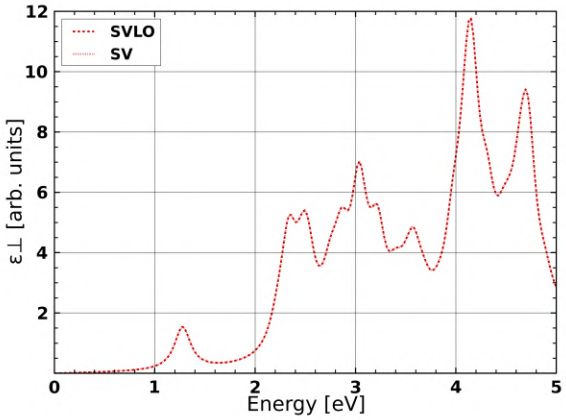

(b) Out-of-plane singlet spectra: SVLO vs SV

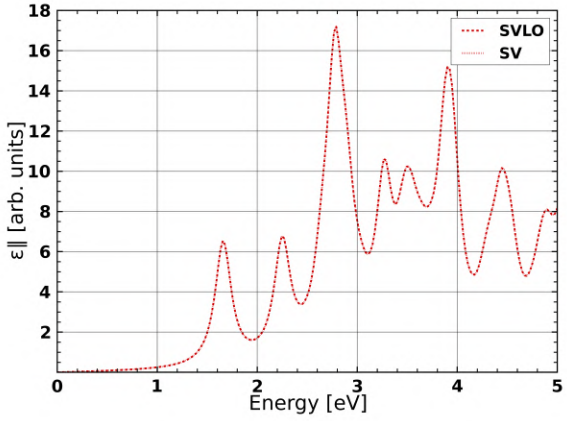

(c) In-plane RPA spectra: SVLO vs SV

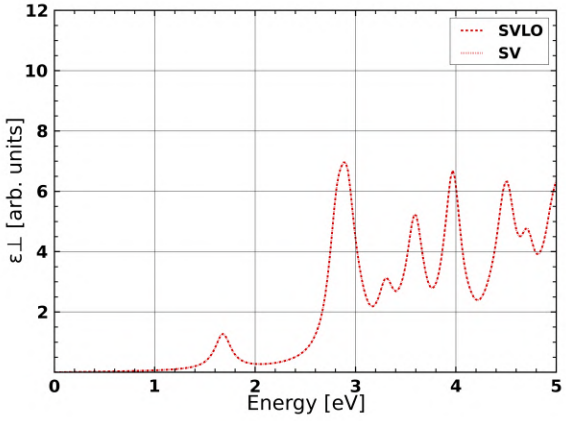

(d) Out-of-plane RPA spectra: SVLO vs SV

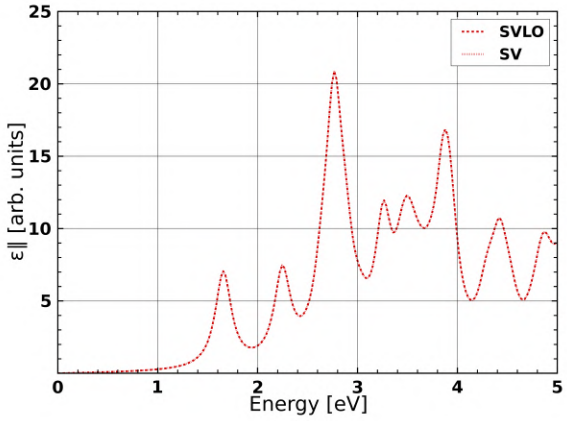

(e) In-plane IP spectra: SVLO vs SV

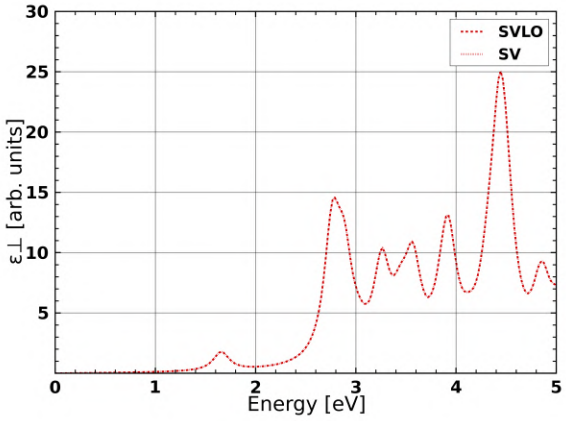

(f) Out-of-plane IP spectra: SVLO vs SV

Figure 4.3: Optical absorption spectra of PbI_2 comparing SVLO and SV methods. (a,b) Singlet exciton spectra showing perfect agreement between SVLO and SV. (c,d) RPA spectra exhibiting identical results. (e,f) IP spectra with matching absorption edges.

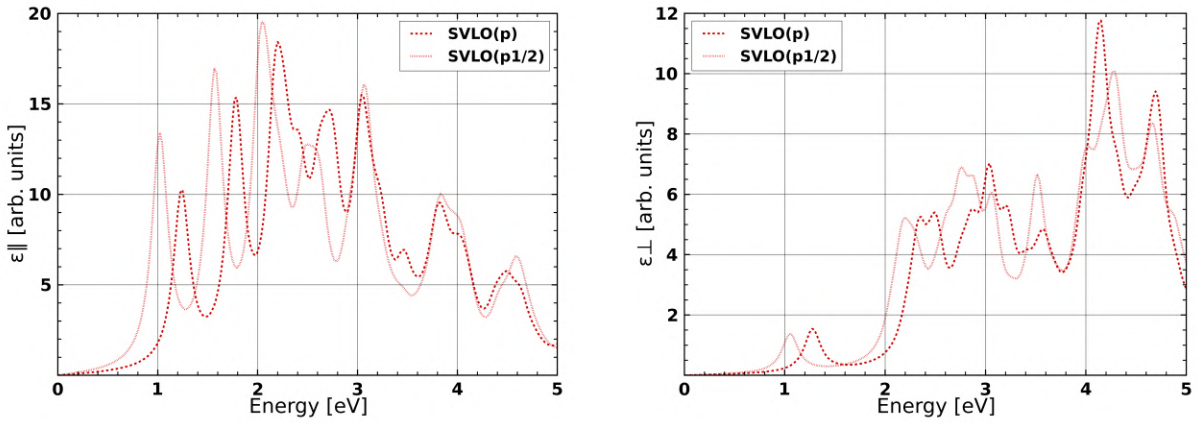

(a) In-plane singlet spectra: SVLO($p_{1/2}$) vs SVLO(p)

(b) Out-of-plane singlet spectra: SVLO($p_{1/2}$) vs SVLO(p)

Figure 4.4: Comparison of SVLO singlet spectra with standard p-type and Dirac-type $p_{1/2}$ local orbitals showing the effect of improved relativistic treatment. (a) In-plane polarization. (b) Out-of-plane polarization.

1.23 eV using only 50 states for $\langle xs \rangle$ *nempty* and $\langle screen \rangle$ *nempty* parameters. The SV method, however, follows a slower trend towards convergence, taking 400 states to reach comparable precision.

Table 4.4: Computational requirements and converged energies for PbI_2 BSE calculations

Method	**Approximation**	$\langle xs \rangle$ *nempty*	$\langle screen \rangle$ *nempty*	**Exciton Energy (eV)**
	Singlet	50	50	1.23
SVLO(p)	RPA	50	—	1.66
	IP	50	—	1.66
SVLO($p_{1/2}$)	Singlet	50	50	1.01
	Singlet	400	400	1.23
SV(p)	RPA	400	—	1.66
	IP	400	—	1.66

The reduction of computational demand achieved by SVLO, from 400 empty states to as few as 50, is directly due to the explicit inclusion of local orbitals in the second variational step. Local orbitals, particularly when chosen to optimally describe relativistic character near heavy nuclei, provide the variational flexibility necessary to model SOC effects without requiring a large number of empty states. In the case of PbI_2, with its strong SOC from Pb atoms, this advantage is particularly significant, demonstrating the usefulness of the SVLO approach in materials where conventional methods become computationally prohibitive[3].

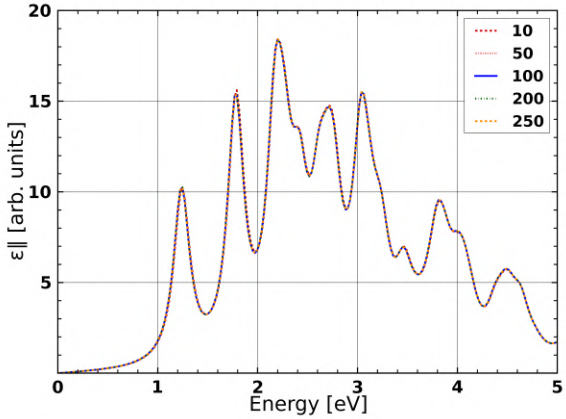

(a) SVLO singlet spectra convergence with $\langle xs \rangle$ *nempty*

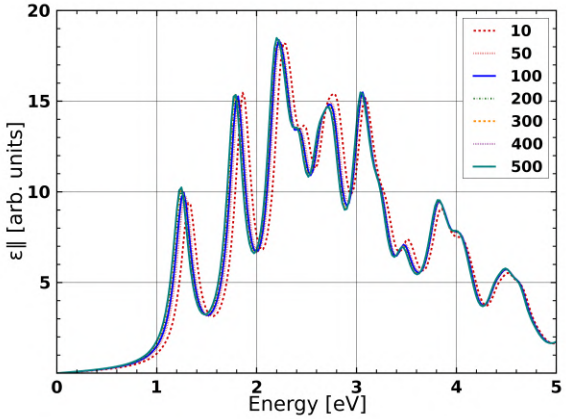

(b) SV singlet spectra convergence with $\langle xs \rangle$ *nempty*

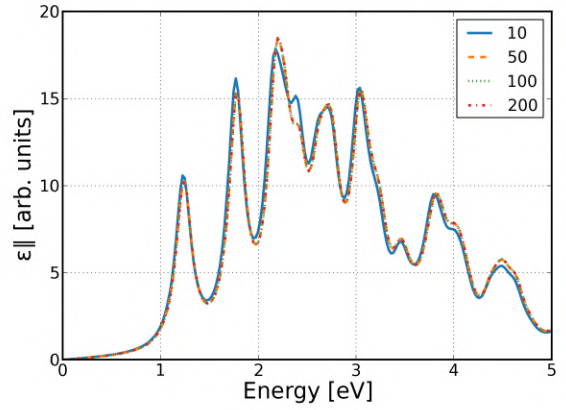

(c) SVLO singlet spectra convergence with $\langle screen \rangle$ *nempty*

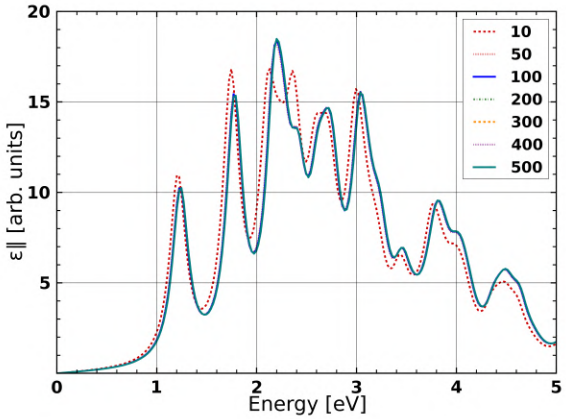

(d) SV singlet spectra convergence with $\langle screen \rangle$ *nempty*

Figure 4.5: Convergence of singlet optical spectra of PbI_2 with respect to $\langle xs \rangle$ *nempty*. (a,c) SVLO converges with 50 empty states. (b,d) SV takes 400 empty states for similar convergence.

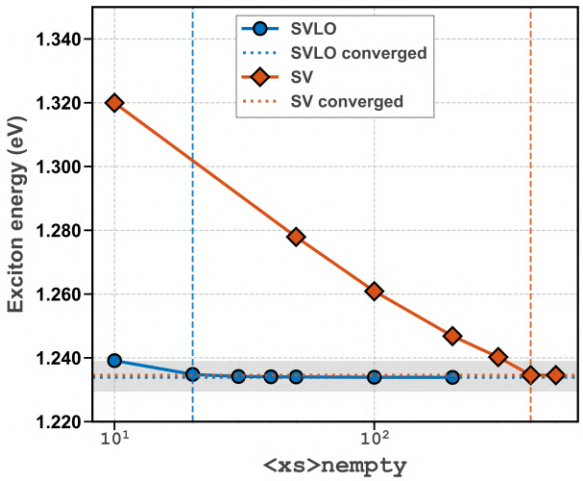

(a) Singlet exciton energy vs $\langle xs \rangle$ *nempty*

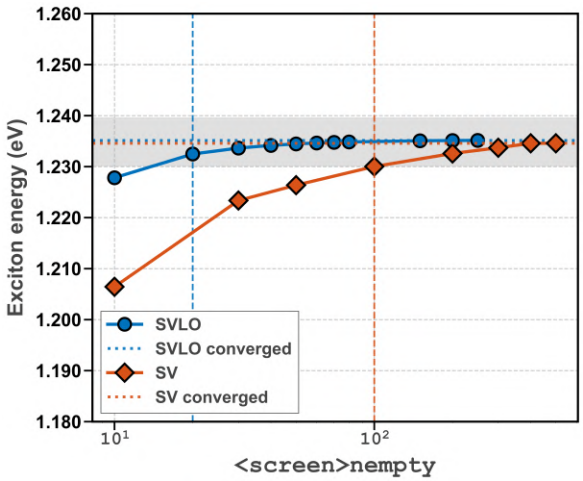

(b) Singlet exciton energy vs $\langle screen \rangle$ *nempty*

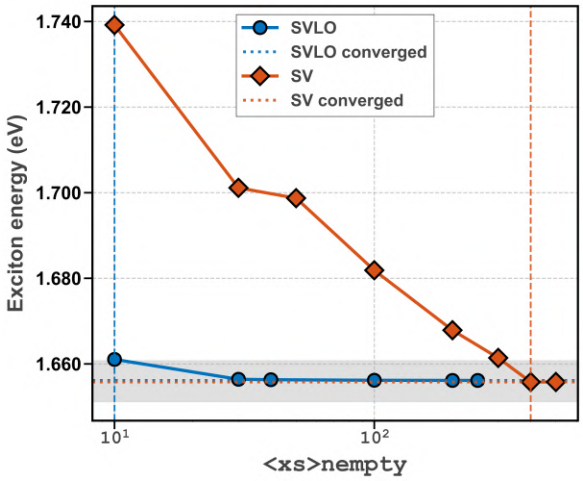

(c) IP exciton energy convergence

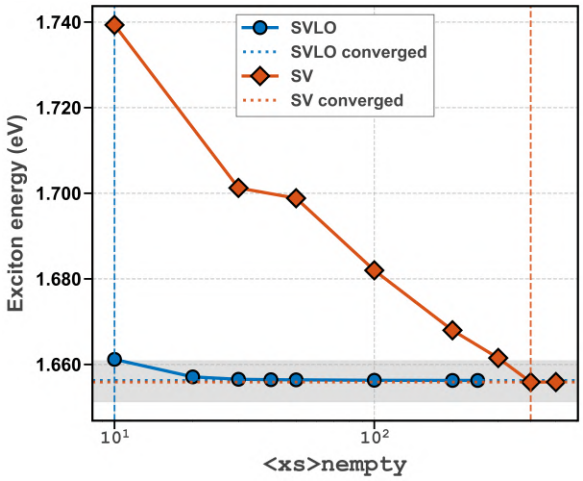

(d) RPA exciton energy convergence

Figure 4.6: Convergence of excitonic energy levels for PbI_2. (a) Singlet exciton with $\langle xs \rangle$ *nempty*. (b) Singlet exciton with $\langle screen \rangle$ *nempty*. (c,d) Convergence of IP and RPA exhibiting similar features between SVLO and SV at 1.66 eV.

4.7 $CsPbI_3$

Cesium lead iodide ($CsPbI_3$) in its γ-phase represents a critical benchmark for establishing the SVLO-BSE implementation in compounds with very strong spin-orbit coupling. As a 3D halide perovskite, $CsPbI_3$ includes heavy lead atoms that are accountable for huge SOC effects and is thus the most demanding computational system for conventional BSE approaches. The material is highly relevant technologically because it can be utilized in photovoltaics and light-emitting devices [39]. The strong SOC effects in $CsPbI_3$ originate primarily from the heavy Pb atoms, where the 6p orbitals experience significant relativistic corrections. The effects lead to drastic changes in the electronic band structure, including narrowing of the band gap and orbital mixing that cannot be adequately described without appropriate relativistic considerations. The three-dimensional perovskite network of corner-sharing PbI_6 octahedra in the γ phase is an ideal platform to study how SOC influences optical excitations in three-dimensional systems [40]. For more detail on the electronic structure from the ground state calculation, see [3]. In the SVLO setups used here, we distinguish two local-orbital variants: SVLO(p), which uses the standard p-type local orbitals on the heavy atoms, and SVLO($p_{1/2}$), which augments the basis with Dirac-type $p_{1/2}$ local orbitals on Pb and I as in [3]. This enlarges the second-variation space and improves the relativistic description of band edges with only a moderate increase in the basis size. Figure 4.7 illustrates the very good agreement between the SVLO and SV methods employed in singlet exciton calculations. The spectra show perfect agreement over the shown energy range, with the first excitonic peak at 0.64 eV, and additional features extending up to 3 eV. The spectral shape has numerous excitonic peaks characteristic of the complicated electronic structure typical of halide perovskites, where multiple valence and conduction bands contribute to the optical response [41].

Including Dirac-type $p_{1/2}$ local orbitals on Pb and I systematically red-shifts the first bright exciton from 0.64 eV to 0.39 eV. Physically, $p_{1/2}$ LOs restore the correct small-r behavior of relativistic $6p_{1/2}$ spinors at heavy nuclei, thereby strengthening the spin–orbit splitting at the band edge [3, 42, 43].

The IP approximation shows the absorption edge at 0.82 eV, corresponding to the fundamental band gap. The RPA spectra, including local-field effects but no electron–hole coupling, keep the first onset at $0.82\ \mathrm{eV}$ while redistributing oscillator strength relative to IP. The full singlet calculation yields the first exciton at 0.64 eV, resulting in a binding energy of 0.18 eV. This relatively small binding energy is characteristic of three-dimensional halide perovskites, reflecting the balance between Coulomb attraction and the comparatively high dielectric screening in the perovskite bulk material [44].

The spectral convergence behavior displayed in Figure 4.9 gives perspective on the improvement in efficiencies by the SVLO approach. In (a) and (b), comparing the convergence with respect to $\langle xs \rangle$ $nempty$ reveals that the SVLO approach shows much faster convergence. The spectra calculated using 200 empty states (blue solid line) within the SVLO scheme are essen-

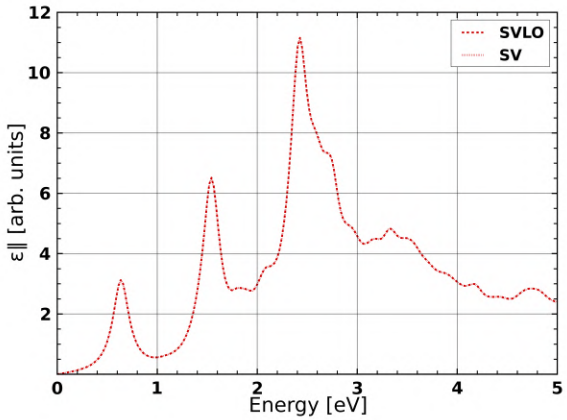

(a) In-plane singlet spectra: SVLO vs SV

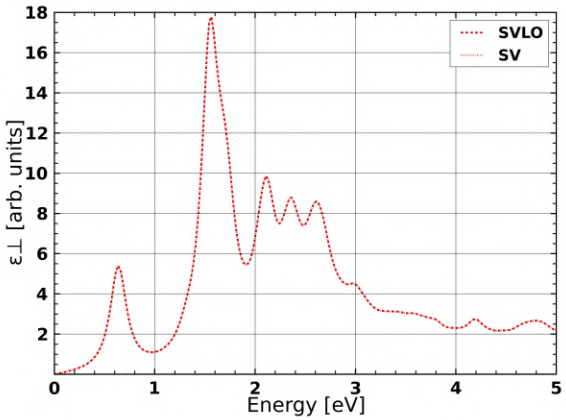

(b) Out-of-plane singlet spectra: SVLO vs SV

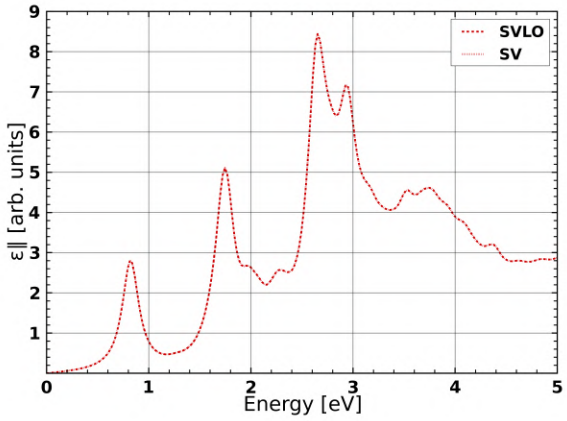

(c) In-plane RPA spectra: SVLO vs SV

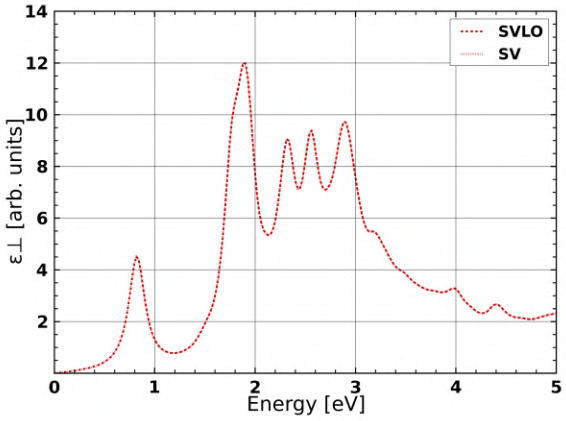

(d) Out-of-plane RPA spectra: SVLO vs SV

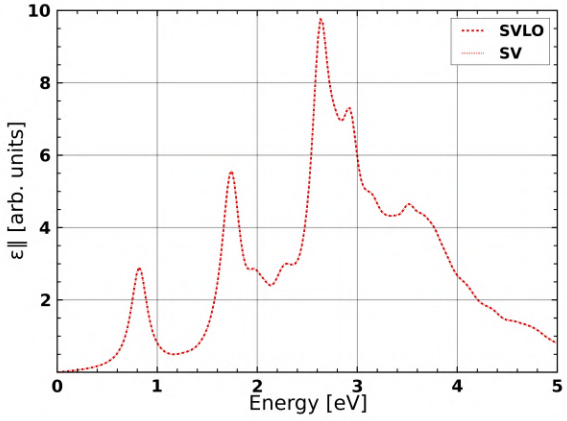

(e) In-plane IP spectra: SVLO vs SV

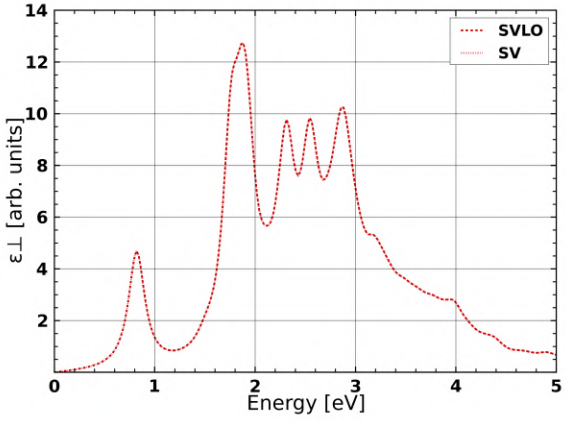

(f) Out-of-plane IP spectra: SVLO vs SV

Figure 4.7: Optical absorption spectra of $CsPbI_3$ comparing SVLO and SV methods. (a,b) Singlet BSE; (c,d) RPA; (e,f) IP.

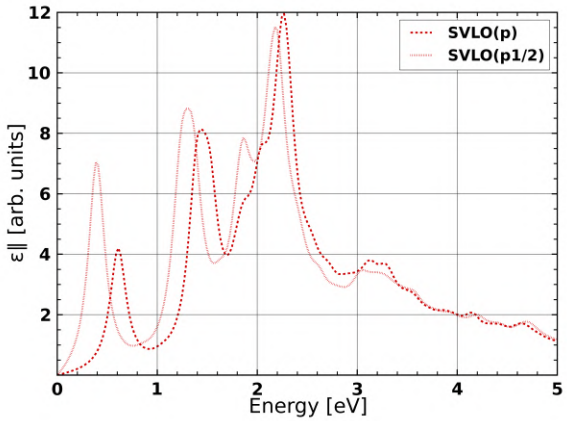

(a) In-plane singlet: SVLO($p_{1/2}$) vs SVLO(p)

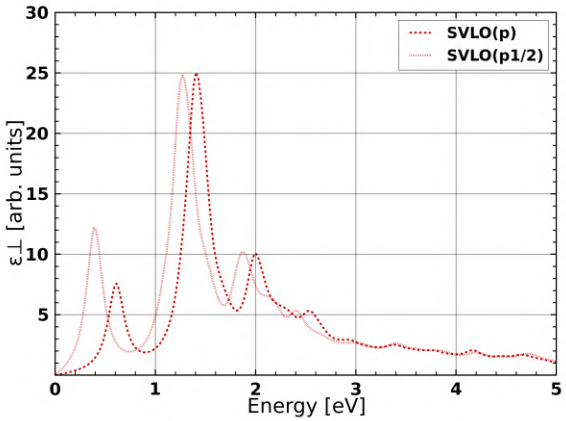

(b) Out-of-plane singlet: SVLO($p_{1/2}$) vs SVLO(p)

Figure 4.8: Effect of Dirac-type $p_{1/2}$ local orbitals on $CsPbI_3$ singlet spectra.

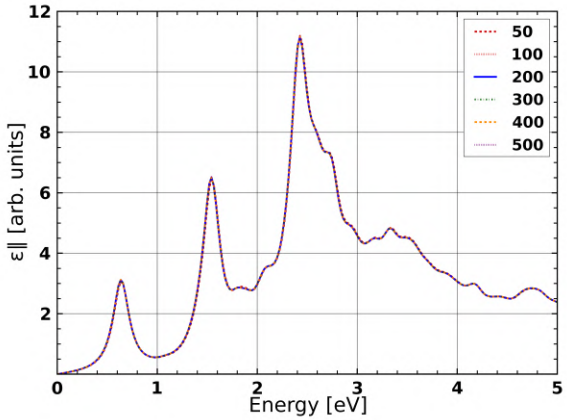

(a) SVLO: spectra vs $\langle xs \rangle$ *nempty*

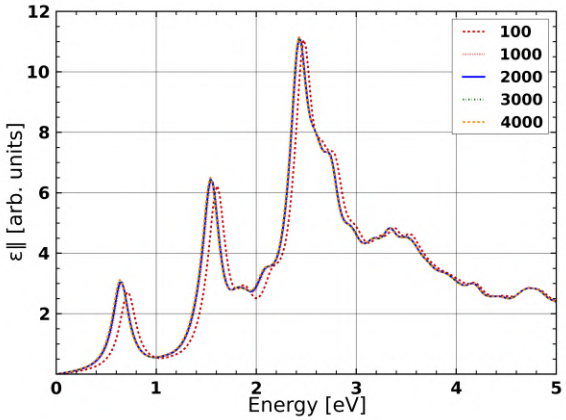

(b) SV: spectra vs $\langle xs \rangle$ *nempty*

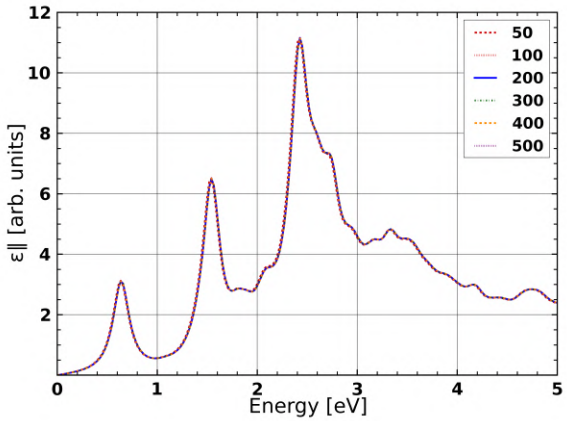

(c) SVLO: spectra vs $\langle screen \rangle$ *nempty*

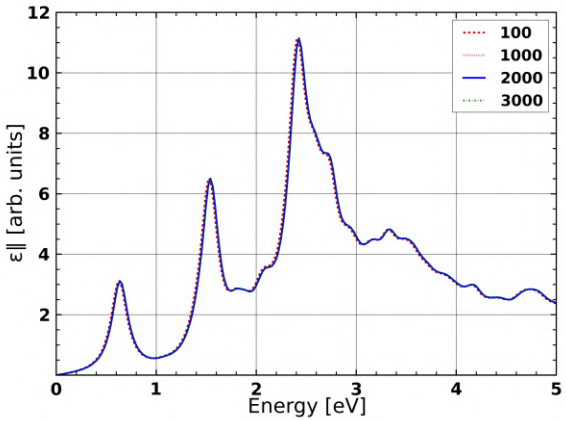

(d) SV: spectra vs $\langle screen \rangle$ *nempty*

Figure 4.9: Convergence of singlet BSE spectra for $CsPbI_3$.

tially indistinguishable from those calculated using 500 states, signaling complete convergence. In stark contrast, the SV approach exhibits large fluctuations even when comparing 3000 and 4000 states, especially in the relative intensities of peaks higher than 2 eV. In addition, the position of the first excitonic peak converges at a much slower rate in the SV approach, slowly moving from around 0.62 eV with 100 states to a converged position of 0.64 eV.

The convergence comparison for screening in panels (c) and (d) shows the same trends. The SVLO approach obtains well-converged spectra with 300 states in the $\langle screen \rangle$ *nempty* parameter, with comparatively modest peak intensity fluctuations at high energies. The SV approach, on the other hand, needs an order of magnitude greater number of states to achieve a similar convergence. Such a substantial decrease in computational demands is especially important for screening calculations, which entail the numerically costly calculation of the dielectric function and screened Coulomb interaction.

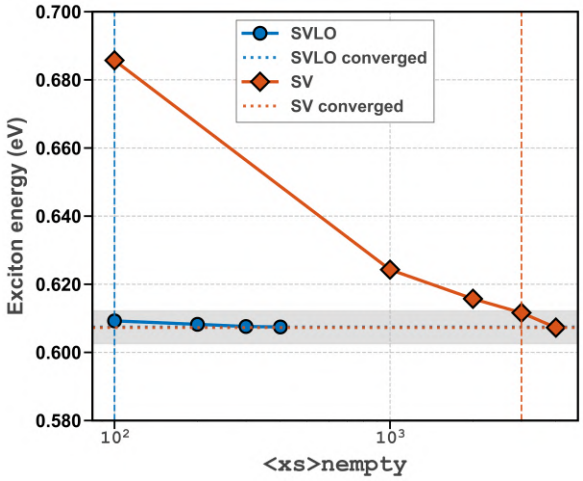

(a) Singlet exciton energy vs $\langle xs \rangle$ *nempty*

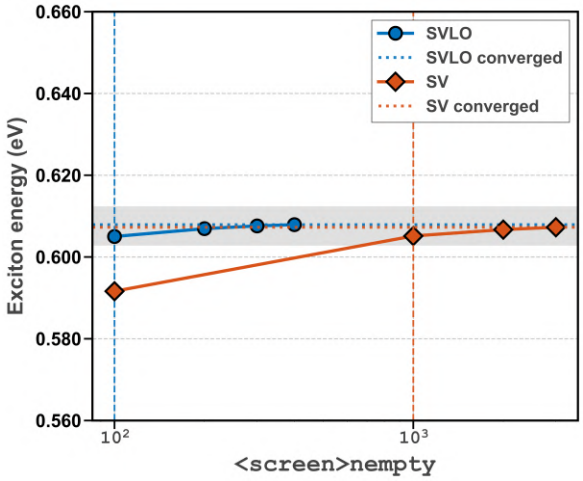

(b) Singlet exciton energy vs $\langle screen \rangle$ *nempty*

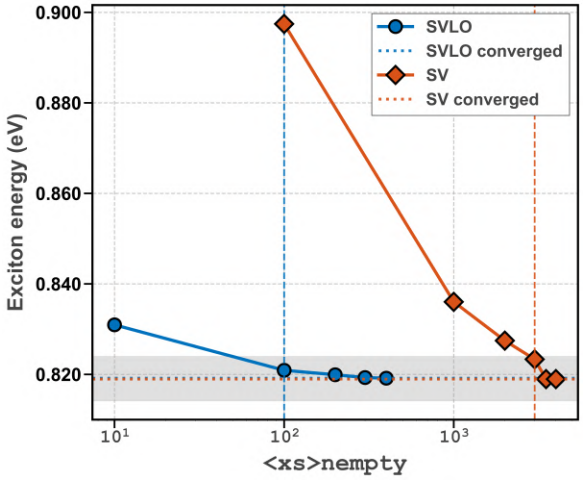

(c) RPA exciton energy vs $\langle xs \rangle$ *nempty*

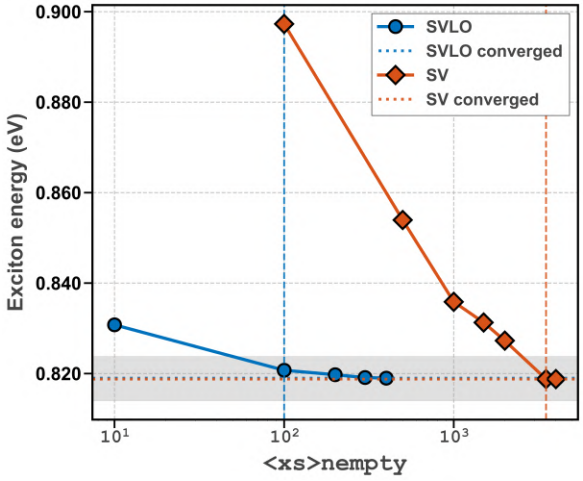

(d) IP exciton energy vs $\langle xs \rangle$ *nempty*

Figure 4.10: Exciton energy convergence for $CsPbI_3$.

The convergence study of $CsPbI_3$ shows that the SVLO method has the most significant gains in efficiency among all the materials studied. As seen from Figure 4.10(a), the SVLO

approach converges at the first excitonic peak of 0.64 eV for singlet exciton calculations using about 200 unoccupied states in the $\langle xs \rangle$ *nempty* parameter. As shown, the SV needs as much as 4000 empty states to obtain the same accuracy, demonstrating an enormous computational cost saving.

The convergence in screening, as shown in Figure 4.10(b), is also converged by the same enhancement in efficiency. The SVLO method converges with approximately 300 empty states with respect to the $\langle screen \rangle$ *nempty* parameter versus the SV method, which requires approximately 3000 states. This huge difference is evidence of the greater capability of the SVLO method in capturing the important physics to strong SOC with a reduced basis set.

The convergence behavior of the RPA and IP approaches, as shown in Figure 4.10(c,d), is analogous. Both approaches show fast convergence with the SVLO method at the 0.82 eV, whereas the SV approach illustrates an extremely slow convergence rate, which demands very large basis sets. The rapid convergence of the SVLO procedure reflects an accurate description of the SOC-deformed electronic states due to the explicit incorporation of local orbitals within the second variational step.

The optical properties of $CsPbI_3$ can be understood by the electronic structure, specifically by the presence of I 5p and Pb 6s states at the band edges. The intense spin-orbit coupling intrinsic to lead atoms is accountable for the high degree of hybridization of these orbitals. The comparatively lower excitonic binding energy with respect to that observed in lower-dimensional perovskites is attributable to the three-dimensional nature of the material, in which the charge carriers have isotropic Coulomb interactions and larger dielectric screening [39].

Some of the excitonic features present in the spectra are due to valence to conduction band transitions, strongly affected by SOC. The perfect agreement between these complex spectral features from both SVLO and SV approaches and the computational efficiency of SVLO is evidence of the correctness of the implementation and usefulness of the technique for the study of halide perovskite compounds.

Table 4.5: Computational requirements and converged energies for $CsPbI_3$ BSE calculations

Method	**Approximation**	$\langle xs \rangle$ *nempty*	$\langle screen \rangle$ *nempty*	**Exciton Energy (eV)**
	Singlet	200	300	0.64
SVLO(p)	RPA	200	—	0.82
	IP	200	—	0.82
SVLO($p_{1/2}$)	Singlet	200	300	0.39
	Singlet	4000	3000	0.64
SV	RPA	4000	—	0.82
	IP	4000	—	0.82

The results on $CsPbI_3$ illustrate the most powerful evidence of the merits of the SVLO method

for materials with strong spin-orbit coupling. Being able to cut computational costs by an order of magnitude, without compromising on detailed accuracy, provides new opportunities for research into the optical properties of halide perovskites and other materials containing heavy atoms, where the spin-orbit coupling is instrumental in establishing their electronic and optical properties. In practice, SVLO reduced the computational cost from 2,298 to 61.6 core-hours by saving 97.5% of the time. Therefore we can verify significant cost efficiency by using SVLO method for massive system.

4.8 Cs_2PbI_4

Cs_2PbI_4 (n=1) is a quasi-two-dimensional Pb–I perovskite in which strong spin–orbit coupling (SOC) from heavy Pb and I atoms governs the band-edge states and excitonic response. We adopt the relaxed structure reported by Maurer *et al.* and use it as input to `exciting` [28]. In such layered Pb–I frameworks, inversion-symmetry breaking together with strong SOC can induce Rashba/Dresselhaus-type features near the band edges; our SVLO–BSE workflow keeps these SOC-modified states consistently from the ground state to the optical step [28]. In the following, SOC is included by SVLO at the DFT level and the resulting spinor states are used for the singlet BSE.

Figure 4.11 shows excellent agreement between SVLO and SV in both polarizations and approximations. From the converged curves we obtain a lowest exciton near 0.891 eV and IP/RPA exciton energy near 1.717 eV, i.e. a binding energy of about 0.83 eV—consistent with strong Coulomb binding and reduced screening in layered perovskites.

For completeness, the numerical values used in the discussion are collected in Table 4.6. For all approximations (singlet BSE/IP/RPA), the two workflows agree on the converged energies within a few meV, while SVLO attains this accuracy with substantially fewer empty states.

Table 4.6: Converged energies and empty-state cutoffs for Cs_2PbI_4

Method	**Approximation**	$\langle xs \rangle$ *nempty*	$\langle screen \rangle$ *nempty*	**Exciton Energy (eV)**
SVLO	Singlet	300	300	0.891
SVLO	RPA	300	–	1.717
SVLO	IP	300	–	1.717
SV	Singlet	1200	1200	0.891
SV	RPA	1200	–	1.717
SV	IP	1200	–	1.717

Through Cs_2PbI_4, we demonstrate that both the SVLO and SV yield the same converged absorption spectra and exciton energies, while SVLO reaches convergence with $\sim 4\times$ fewer empty states in both the transition basis and the screening. Together with the large binding energy ($\sim$0.83 eV) characteristic of the n=1 layered geometry, this shows that SVLO preserves spectral accuracy while substantially reducing numerical cost in SOC-dominated 2D perovskites.

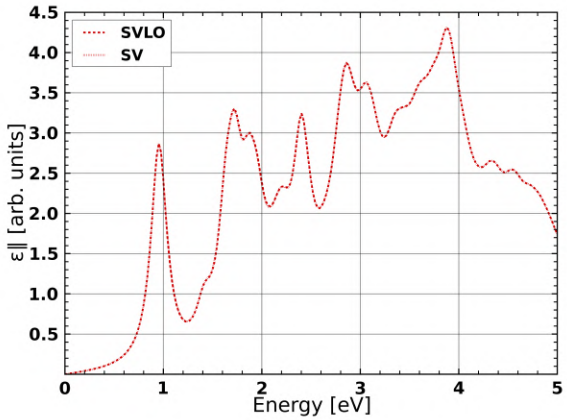

(a) In-plane singlet: SVLO vs SV

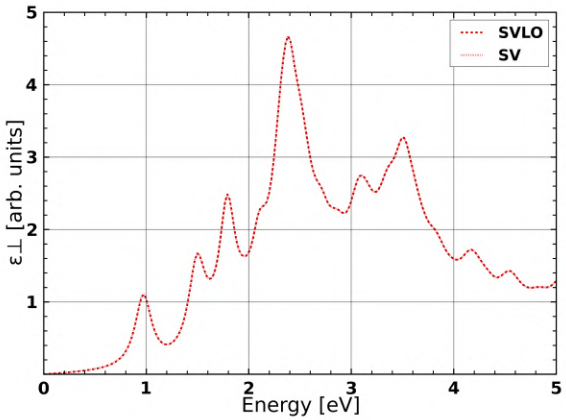

(b) Out-of-plane singlet: SVLO vs SV

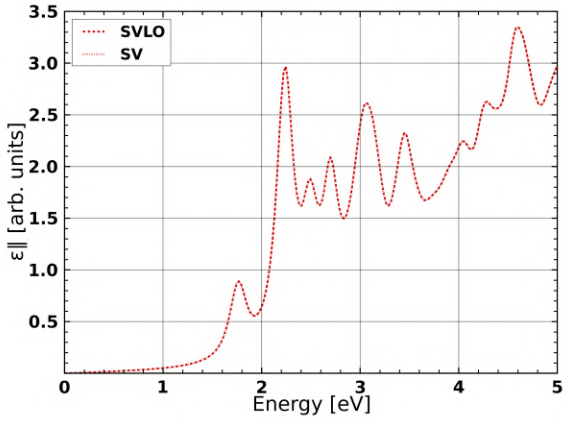

(c) In-plane RPA: SVLO vs SV

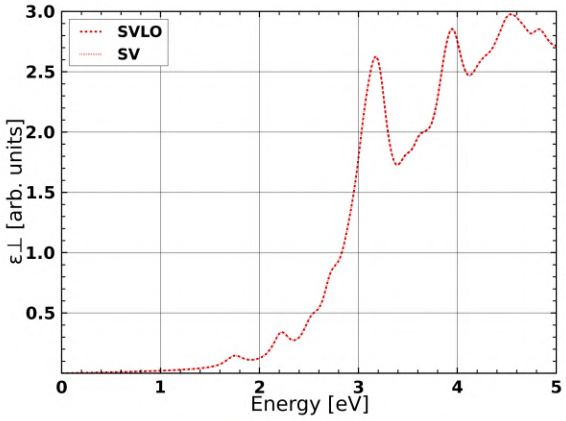

(d) Out-of-plane RPA: SVLO vs SV

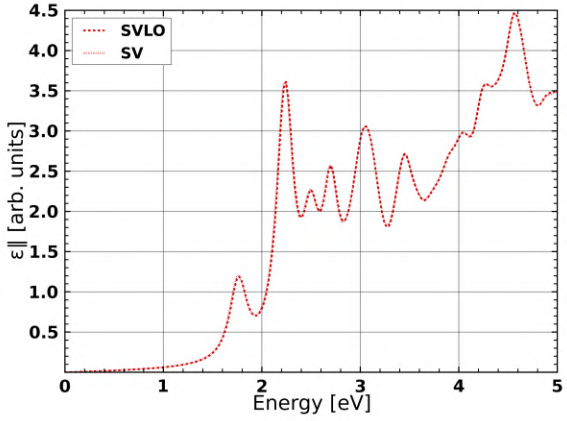

(e) In-plane IP: SVLO vs SV

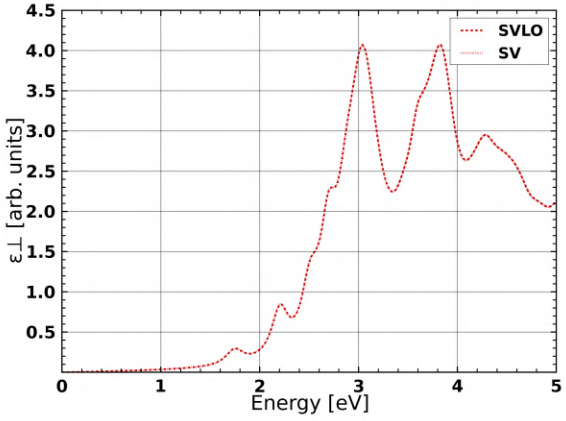

(f) Out-of-plane IP: SVLO vs SV

Figure 4.11: Optical absorption spectra of Cs_2PbI_4, comparing SVLO and SV. (a,b) Singlet BSE; (c,d) RPA; (e,f) IP.

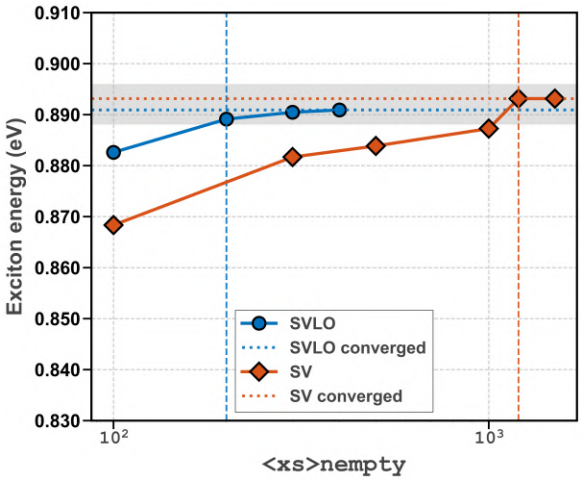

(a) Singlet (BSE): exciton energy vs $\langle xs \rangle$ *nempty*

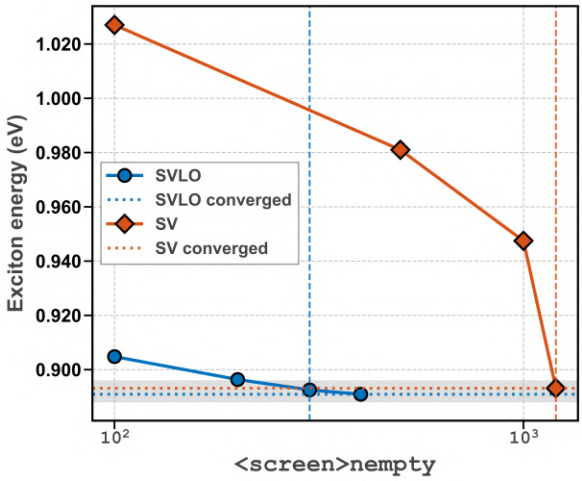

(b) Singlet (BSE): exciton energy vs $\langle screen \rangle$ *nempty*

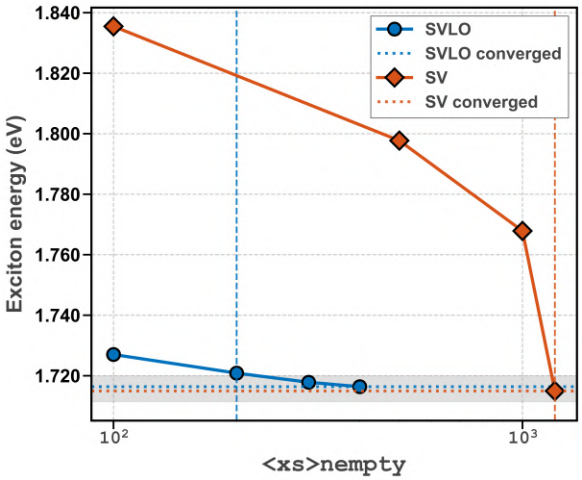

(c) IP: exciton energy vs $\langle xs \rangle$ *nempty*

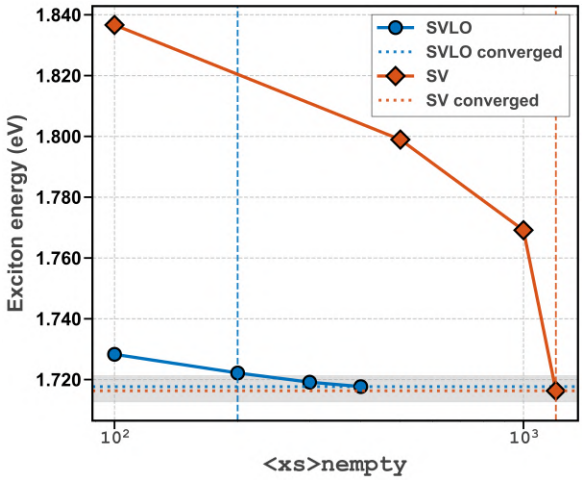

(d) RPA: exciton energy vs $\langle xs \rangle$ *nempty*

Figure 4.12: Convergence of characteristic energies in Cs_2PbI_4 with SVLO and SV.

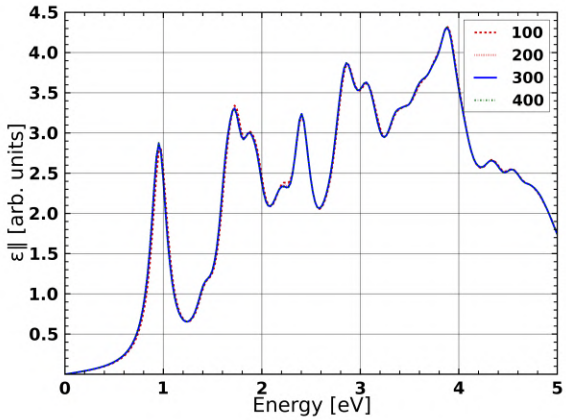

(a) SVLO: spectra vs $\langle xs \rangle$ *nempty*

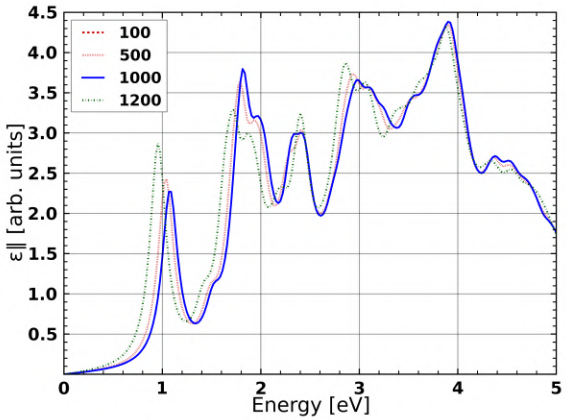

(b) SV: spectra vs $\langle xs \rangle$ *nempty*

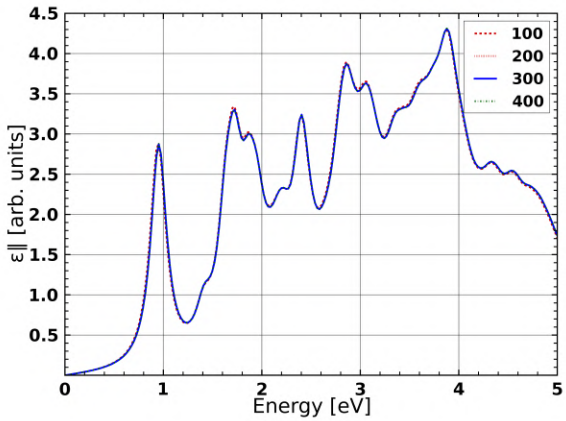

(c) SVLO: spectra vs $\langle screen \rangle$ *nempty*

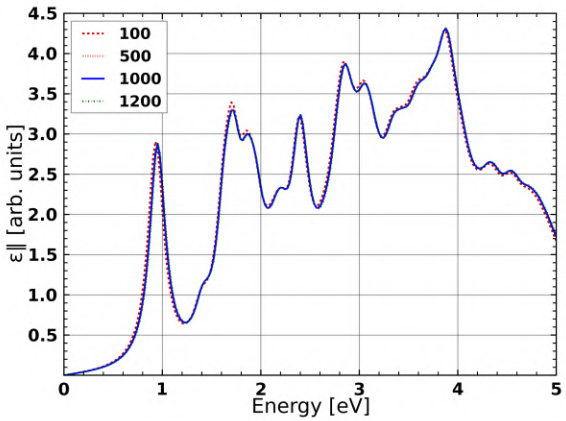

(d) SV: spectra vs $\langle screen \rangle$ *nempty*

Figure 4.13: Convergence of singlet BSE spectra for Cs_2PbI_4.

4.9 $Cs_4AgBiBr_8$

$Cs_4AgBiBr_8$ is a lead-free, two-dimensional (2D) all-inorganic double perovskite of the Ruddlesden–Popper (RP) type. Due to its layered RP architecture and the Ag/Bi cation ordering, it has attracted attention as an environmentally friendly perovskite with pronounced excitonic effects and potential in light-emission applications [29, 30]. We adopt the PBE-optimized RP structure reported by Chen *et al.* as the starting point for all-electron LAPW+lo calculations in `exciting` [4, 29]. Their VASP/PAW benchmarks (PBE + SOC) place the band gap at 1.45 eV and explicitly characterize $Cs_4AgBiBr_8$ as a 2D RP double perovskite, providing a convenient DFT reference for comparison [29].

Within our SVLO workflow (Sec. 2), we converged the ground state including SOC. Using the SVLO basis with standard p-type local orbitals [SVLO(p)] on a $6 \times 6 \times 1$ k-grid, we obtain a PBE + SOC quasiparticle (QP) gap (E_{gap}) of 1.579 eV. This value is slightly larger than the VASP/PAW value, which is a well-documented deviation of $\mathcal{O}(10^{-1})$ eV between all-electron and pseudopotential methods in halide perovskites [4, 45]. When Dirac-type $p_{1/2}$ local orbitals are added on the relevant p manifolds [SVLO($p_{1/2}$)] on the same $6 \times 6 \times 1$ grid, the gap reduces significantly to 1.350 eV. The net lowering by ~ 0.23 eV mirrors the trend established above for PbI_2 and $CsPbI_3$: explicitly resolving the near-nucleus j-dependence via $p_{1/2}$ LOs sharpens the SOC description and yields quantitatively more reliable gaps in heavy-p systems [3].

Numerically, the excitonic transition space constructed from these spinor states is large, with the $6 \times 6 \times 1$ grid already resulting in a BSE Hamiltonian of dimension $N \approx 7020$. Despite this overall size, convergence with respect to empty bands was reached with only $\langle xs \rangle$ *nempty* = 300 (and $\langle screen \rangle$ *nempty* = 300), i.e., a small fraction of the total space. Consistent with our other strong-SOC test cases, this demonstrates that the explicitly added LOs in SVLO effectively reduce the required number of empty states without losing the near-gap accuracy [3]. These converged ground state calculations form the inputs for subsequent BSE calculations on this RP double perovskite.

We applied this SVLO-BSE workflow to both basis sets on the $6\times6\times1$ k-grid. For the standard 'SVLO(p)' basis, we find the first bright excitonic peak (E_1) at 0.691 eV. With the corresponding QP gap of 1.579 eV, this yields an exciton binding energy of $E_b = E_{\mathrm{gap}} - E_1 \approx 0.887$ eV (887 meV). Using the more accurate 'SVLO(p1/2)' basis, E_1 is found at 0.512 eV over its corresponding QP gap of 1.350 eV. This gives a binding energy of $E_b \approx 0.838$ eV (838 meV). This comparison is critical: it demonstrates that the inclusion of Dirac-type LOs not only lowers the QP gap (by ~ 0.23 eV) but also directly impacts the excitonic calculation, reducing the computed binding energy by ~ 50 meV.

Figure 4.14 summarizes the polarization dependence. In panel 4.14a, the two basis choices produce nearly identical in-plane line shapes with a modest redshift for SVLO($p_{1/2}$), matching the reduction in E_{gap}. Panel 4.14b highlights the pronounced anisotropy: $\varepsilon_\perp$ remains weak at low energies and increases only at higher photon energies, as expected for layered RP

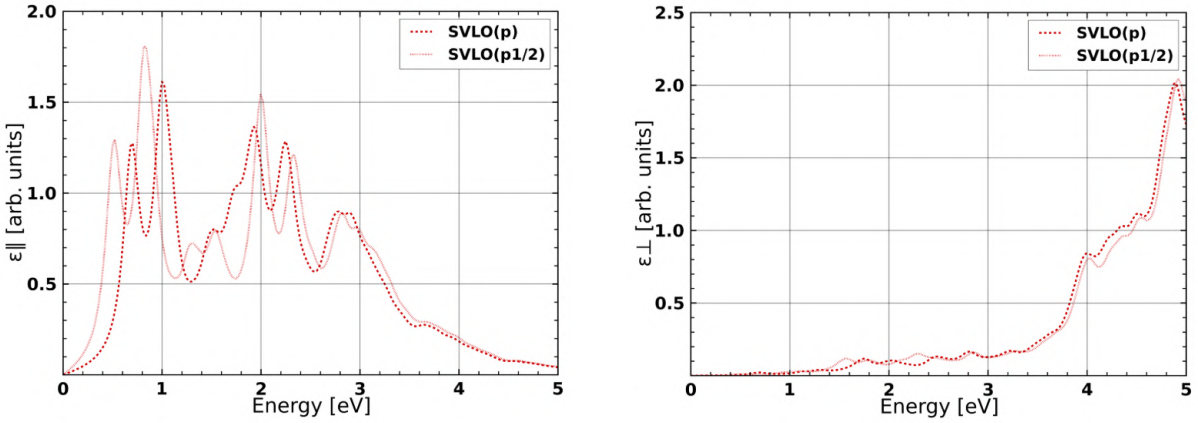

(a) In-plane response $\varepsilon_{\parallel}(\omega)$ from singlet BSE comparing SVLO(p) and SVLO$(p_{1/2})$.

(b) Out-of-plane response $\varepsilon_{\perp}(\omega)$ from singlet BSE comparing SVLO(p) and SVLO$(p_{1/2})$.

Figure 4.14: Optical absorption spectra of $Cs_4AgBiBr_8$ at the singlet BSE level. (a) in-plane (b) out-of-plane. SVLO(p) and SVLO$(p_{1/2})$ give essentially identical spectra over the shown range, with a slight redshift for $p_{1/2}$.

perovskites with strong out-of-plane confinement and reduced interlayer coupling [29, 30].

These binding energies (840–890 meV) must be interpreted with caution. It is well-known that coarse k-grids (like $6 \times 6 \times 1$) in 2D materials tend to insufficiently sample the $\mathbf{q} \to 0$ region of the Coulomb interaction, often leading to an artificial overestimation of the binding energy[41, 46]. This numerical artifact likely competes with the systematic underestimation of E_b from the BSE@PBE+SOC theoretical level, which overestimates screening. Therefore, while we have successfully validated the efficiency of the SVLO-BSE workflow and the physical importance of Dirac-type LOs, a quantitatively converged E_b would require a much denser k-point mesh[41, 46].

As for material context, prior VASP studies on the Cs_4AgBiX_8 series emphasize its RP layering, 2D charge confinement, and comparatively large exciton binding energies, which together point to applications in luminescent devices rather than photovoltaics [29, 30]. Our all-electron SVLO results. which confirm a large, sub-gap exciton peak, are consistent with this picture, while highlighting the quantitative role of Dirac-type LOs for SOC-dominated band edges.

5 Conclusion

This thesis extends the second-variational with local orbitals (SVLO) strategy to the Bethe–Salpeter equation (BSE) workflow for optical spectra of materials with strong spin-orbit coupling (SOC). The implementation computes, within a spinor formalism, the momentum matrix elements that set oscillator strengths and the plane-wave transition-density matrix elements that enter the screened direct and bare-exchange kernels. The construction treats SOC consistently within the SVLO transformation and employs the standard static screening $W(\omega = 0)$ and the resonant block of the BSE operator.

Across all results, the SVLO-BSE spectra agree with the standard second-variational (SV) results at convergence while requiring far fewer empty states. For the 2D semiconductor MoS_2 with moderate SOC, SVLO reproduces the SV line shape and exciton positions within a few meV; the first bright exciton appears near $0.95\ \mathrm{eV}$ and the independent-particle (IP)/RPA onset near $1.70\ \mathrm{eV}$, giving a large binding energy characteristic of weak dielectric screening in 2D. The near-perfect overlap between SVLO and SV in both polarization channels verifies reproducibility in a regime where SOC is not the limiting numerical factor.

The efficiency gain of SVLO is decisive in heavy-atom systems. In layered PbI_2, singlet BSE spectra converge with $\langle xs \rangle\ nempty \approx 50$ for SVLO, whereas SV needs about 400 states to stabilize both the first peak at $1.23\ \mathrm{eV}$ and the higher-energy features. A similar reduction holds for the screening cutoff, $\langle screen \rangle\ nempty$. Including Dirac-type $p_{1/2}$ local orbitals slightly reduces the gap and produces a small, systematic redshift at fixed convergence, consistent with the improved near-nucleus j-resolved radial behavior.

In bulk γ-$CsPbI_3$, SVLO reduces required number of empty states by roughly an order of magnitude: $\langle xs \rangle\ nempty \sim 200$ vs ~ 4000 unoccupied states for the transition space and $\langle screen \rangle\ nempty \sim 300$ vs ~ 3000 for the screening, yet both workflows yield an exciton at $0.64\ \mathrm{eV}$ and an IP/RPA onset at $0.82\ \mathrm{eV}$. The modest binding energy reflects the larger 3D screening, while the drastic numerical savings show that explicitly adding physically targeted local orbitals captures SOC-induced changes in near-edge states.

For the layered perovskite Cs_2PbI_4 ($n = 1$), SVLO and SV produce indistinguishable converged spectra and energies while SVLO reaches stability with $\langle xs \rangle\ nempty \approx 300$ and $\langle screen \rangle\ nempty \approx 300$, versus $\gtrsim 1000$–1200 for SV. The lowest singlet exciton near $0.891\ \mathrm{eV}$ and the IP/RPA onset near $1.717\ \mathrm{eV}$ imply a binding energy of order $0.8\ \mathrm{eV}$, consistent with strong Coulomb attraction and reduced dimensional screening.

Finally, the application to the 2D double perovskite $Cs_4AgBiBr_8$ shows the method's strength.

Using standard p-type local orbitals gives a PBE+SOC gap around $1.57\,\mathrm{eV}$; adding Dirac-type $p_{1/2}$ orbitals lowers it to $\sim 1.36\,\mathrm{eV}$ and the BSE convergence attainable with $\langle xs \rangle\ nempty \approx 300$. This mirrors the Pb/I systems: better near-nucleus relativistic flexibility produces quantitatively improved gaps and faster optical convergence.

Beyond performance, the results sharpen several physical trends. In 2D systems (MoS_2, Cs_2PbI_4), reduced screening yields large exciton binding energies and strong polarization anisotropy; in 3D $CsPbI_3$, stronger screening lowers E_b. The inclusion of Dirac-type $p_{1/2}$ orbitals provides a compact way to encode j-dependent radial structure essential for heavy-p band edges, improving both the ground-state gaps and the stability of near-edge optical features at moderate cutoffs. In summary, the SVLO extension to the BSE workflow reproduces converged SV spectra and exciton energies while reducing the number of empty states by factors of 4 to 20 in SOC-dominated materials. The method delivers accurate results from 2D dichalcogenides to 3D and layered halide perovskites, and it does so at a fraction of the cost. The combination of physical transparency and algorithmic efficiency (smaller N_u) makes SVLO-BSE a practical tool for predictive optical spectroscopy in heavy-element materials. Moreover, explicitly augmenting the SVLO subspace with Dirac-type $p_{1/2}$ local orbitals further improves the relativistic accuracy of near-edge states, yielding small, systematic adjustments of peak positions while preserving the convergence gains and overall lineshapes at convergence.

$$E_b = E_{\mathrm{gap}} - E_1,$$

with E_1 the energy of the lowest bright exciton and E_{gap} the direct quasiparticle gap. Within this definition, the reported bindings and convergence behaviors across MoS_2, PbI_2, $CsPbI_3$, Cs_2PbI_4 and $Cs_4AgBiBr_8$ are internally consistent and align with the dimensional screening trends established in the literature. The $p_{1/2}$ augmentation is especially useful for Pb- and I-based systems, where strong SOC reshapes the p-manifolds near the band edges.

Bibliography

[1] Woncheol Lee et al. “Spin–orbit effects on the electronic and optical properties of lead iodide”. In: *Applied Physics Letters* 122.21 (2023), p. 212110. DOI: 10.1063/5.0146397. URL: https://doi.org/10.1063/5.0146397.

[2] Christiane Vorwerk et al. “Bethe-Salpeter equation for absorption and scattering spectroscopy: Implementation in the exciting code”. In: *arXiv* (2019). eprint: 1909.08366.

[3] Cecilia Vona et al. “Accurate and efficient treatment of spin-orbit coupling via second variation employing local orbitals”. In: *Phys. Rev. B* 108.23 (2023), p. 235161. DOI: 10.1103/PhysRevB.108.235161. URL: https://link.aps.org/doi/10.1103/PhysRevB.108.235161.

[4] Andris Gulans et al. “exciting: a full-potential all-electron package implementing density-functional theory and many-body perturbation theory”. In: *Journal of Physics: Condensed Matter* 26.36 (2014), p. 363202. DOI: 10.1088/0953-8984/26/36/363202. URL: https://dx.doi.org/10.1088/0953-8984/26/36/363202.

[5] Various. “Electronic Structure of (Organic-)Inorganic Metal Halide Perovskites: The Dilemma of Choosing the Right Functional”. In: *Advanced Theory and Simulations* 5.1 (2022), p. 2100496. DOI: 10.1002/adts.202100496.

[6] L. H. Thomas. “The calculation of atomic fields”. In: *Mathematical Proceedings of the Cambridge Philosophical Society* 23.5 (1927), pp. 542–548. DOI: 10.1017/S030500410001168X.

[7] E. Fermi. “Eine statistische Methode zur Bestimmung einiger Eigenschaften des Atoms und ihre Anwendung auf die Theorie des periodischen Systems der Elemente”. In: *Zeitschrift für Physik* 48.1-2 (1928), pp. 73–79. DOI: 10.1007/BF01351576.

[8] P. Hohenberg and W. Kohn. “Inhomogeneous Electron Gas”. In: *Physical Review* 136.3B (1964), B864–B871. DOI: 10.1103/PhysRev.136.B864.

[9] W. Kohn and L. J. Sham. “Self-Consistent Equations Including Exchange and Correlation Effects”. In: *Physical Review* 140.4A (1965), A1133–A1138. DOI: 10.1103/PhysRev.140.A1133.

[10] John P. Perdew, Kieron Burke, and Matthias Ernzerhof. “Generalized Gradient Approximation Made Simple”. In: *Phys. Rev. Lett.* 77.18 (1996), pp. 3865–3868. DOI: 10.1103/PhysRevLett.77.3865.

[11] Felix Bloch. “Über die Quantenmechanik der Elektronen in Kristallgittern”. In: *Zeitschrift für Physik* 52 (1929), pp. 555–600.

[12] David Singh and Lars Nordström. *Planewaves, Pseudopotentials and the LAPW Method, Second Edition*. Springer, 2005. ISBN: 978-0-387-28780-5. DOI: 10.1007/978-0-387-29684-5.

[13] O. Krogh Andersen. “Linear methods in band theory”. In: *Phys. Rev. B* 12.8 (1975), pp. 3060–3083. DOI: 10.1103/PhysRevB.12.3060.

[14] David Singh. “Ground-state properties of lanthanum: Treatment of extended-core states”. In: *Phys. Rev. B* 43.8 (1991), pp. 6388–6392. DOI: 10.1103/PhysRevB.43.6388.

[15] Hannah Kleine et al. “Dirac-type local orbitals for strong SOC materials”. In: (2021). Preprint or online resource.

[16] T. L. Loucks. “Relativistic Electronic Structure in Crystals. I. Theory”. In: *Phys. Rev.* 139.4A (1965), A1333–A1337. DOI: 10.1103/PhysRev.139.A1333.

[17] Andris Gulans and Claudia Draxl. *Influence of spin-orbit coupling on chemical bonding*. 2022. arXiv: 2204.02751 [cond-mat.mtrl-sci].

[18] William P. Huhn and Volker Blum. “One-hundred-three compound band-structure benchmark of post-self-consistent spin-orbit coupling treatments in density functional theory”. In: *Phys. Rev. Mater.* 1.3 (2017), p. 033803. DOI: 10.1103/PhysRevMaterials.1.033803.

[19] Giovanni Onida, Lucia Reining, and Angel Rubio. “Electronic excitations: density-functional versus many-body Green’s-function approaches”. In: *Reviews of Modern Physics* 74.2 (2002), pp. 601–659.

[20] Michael Rohlfing and Steven G Louie. “Electron-hole excitations and optical spectra from first principles”. In: *Physical Review B* 62.8 (2000), pp. 4927–4944.

[21] G. Cappellini et al. “Model dielectric function for semiconductors”. In: *Phys. Rev. B* 47.15 (1993), pp. 9892–9895. DOI: 10.1103/PhysRevB.47.9892.

[22] Stephan Sagmeister. “Excitonic Effects in Solids: Time-Dependent Density Functional Theory versus the Bethe-Salpeter Equation”. Dr. rer. nat. dissertation. Graz, Austria: Karl-Franzens-Universität Graz, Aug. 2009.

[23] Roberto Orlando, Pina Romaniello, and Pierre-François Loos. “Exploring new exchange-correlation kernels in the Bethe–Salpeter equation: A study of the asymmetric Hubbard dimer”. In: *Advances in Quantum Chemistry*. Ed. by Philip E. Hoggan. Vol. 88. Advances in Quantum Chemistry. Academic Press, 2023, pp. 183–211. DOI: 10.1016/bs.aiq.2023.02.007.

[24] D. D. Koelling and B. N. Harmon. "A Technique for Relativistic Spin-Polarized Calculations". In: *Journal of Physics C: Solid State Physics* 10.16 (1977), pp. 3107–3114. DOI: 10.1088/0022-3719/10/16/019.

[25] A. H. MacDonald, W. E. Pickett, and D. D. Koelling. "A Linearised Relativistic Augmented-Plane-Wave Method Utilising Approximate Pure Spin Basis Functions". In: *Journal of Physics C: Solid State Physics* 13.14 (1980), pp. 2675–2683. DOI: 10.1088/0022-3719/13/14/009.

[26] C. C. J. Roothaan. "New Developments in Molecular Orbital Theory". In: *Reviews of Modern Physics* 23.2 (1951), pp. 69–89. DOI: 10.1103/RevModPhys.23.69.

[27] Per-Olov Löwdin. "On the Non-Orthogonality Problem Connected with the Use of Atomic Wave Functions in the Theory of Molecules and Crystals". In: *The Journal of Chemical Physics* 18.3 (1950), pp. 365–375. DOI: 10.1063/1.1747632.

[28] Benedikt Maurer, Christian Vorwerk, and Claudia Draxl. "Rashba and Dresselhaus effects in two-dimensional Pb-I-based perovskites". In: *Phys. Rev. B* 105.15 (2022), p. 155149. DOI: 10.1103/PhysRevB.105.155149.

[29] Yan-Long Chen et al. "2D and 3D double perovskite with dimensionality-dependent optoelectronic properties: first-principle study on Cs2AgBiBr6 and Cs4AgBiBr8". In: *Journal of Physics: Condensed Matter* 34 (2022), p. 065501. DOI: 10.1088/1361-648X/ac34ae.

[30] Ming-Wei Zeng, Yu-Qing Zhao, and Meng-Qiu Cai. "Effects of Halogen Substitution on the Optoelectronic Properties of Two-Dimensional All-Inorganic Double Perovskite Cs4AgBiX8 (X = Cl, Br, I) with Ruddlesden–Popper Structure". In: *Physical Review Applied* 16 (2021), p. 054019. DOI: 10.1103/PhysRevApplied.16.054019.

[31] Hualing Zeng et al. "Control of valley polarization in monolayer MoS2 by optical helicity". In: *Nature Nanotechnology* 7.8 (2012), pp. 490–493.

[32] Qing Hua Wang et al. "Electronics and optoelectronics of two-dimensional transition metal dichalcogenides". In: *Nature Nanotechnology* 8.9 (2013), pp. 699–712.

[33] Alexey Chernikov et al. "Exciton binding energy and nonhydrogenic Rydberg series in monolayer WS2". In: *Physical Review Letters* 113.7 (2014), p. 076802.

[34] Andor Kormányos et al. "k·p theory for two-dimensional transition metal dichalcogenide semiconductors". In: *2D Materials* 2.2 (2015), p. 022001. DOI: 10.1088/2053-1583/2/2/022001.

[35] E. Cappelluti et al. "Tight-binding model and direct-gap/indirect-gap transition in single-layer and multilayer MoS_2". In: *Physical Review B* 88 (2013), p. 075409. DOI: 10.1103/PhysRevB.88.075409.

[36] Gui-Bin Liu et al. “Three-band tight-binding model for monolayers of group-VIB transition metal dichalcogenides”. In: *Physical Review B* 88 (2013), p. 085433. DOI: 10.1103/PhysRevB.88.085433.

[37] Yang Tan et al. “Polarization-dependent optical absorption of MoS_2 for refractive index sensing”. In: *Scientific Reports* 4 (2014), p. 7523. DOI: 10.1038/srep07523.

[38] Daniel Trainer et al. “Inter-Layer Coupling Induced Valence Band Edge Shift in Mono- to Few-Layer MoS_2”. In: *Scientific Reports* 7 (2017), p. 40559. DOI: 10.1038/srep40559.

[39] Shi-yu Yuan et al. “CsPbI3 all-inorganic perovskite solar cells: Development status and theoretical prediction”. In: *Journal of Solid State Chemistry* 336 (2024), p. 124780. DOI: 10.1016/j.jssc.2024.124780.

[40] Xue Tan et al. “Stabilizing CsPbI3 perovskite for photovoltaic applications”. In: *Matter* 6.3 (2023), pp. 691–727. DOI: 10.1016/j.matt.2022.12.012.

[41] Félix Thouin et al. “Enhanced screening and spectral diversity in many-body elastic scattering of excitons in two-dimensional hybrid metal-halide perovskites”. In: *Phys. Rev. Res.* 1.3 (2019), p. 032032. DOI: 10.1103/PhysRevResearch.1.032032.

[42] Jacky Even et al. “Importance of Spin–Orbit Coupling in Hybrid Organic–Inorganic Perovskites for Photovoltaic Applications”. In: *J. Phys. Chem. Lett.* 4.17 (2013), pp. 2999–3005. DOI: 10.1021/jz401532q.

[43] Jan Kuneš et al. “Electronic structure of fcc Th: Spin-orbit calculation with $6p_{1/2}$ local orbital extension”. In: *Physical Review B* 64 (2001), p. 153102. DOI: 10.1103/PhysRevB.64.153102. URL: https://link.aps.org/doi/10.1103/PhysRevB.64.153102.

[44] Nam-Kwang Cho et al. “Long-term stability in γ-$CsPbI_3$ perovskite via an ultraviolet-curable polymer network”. In: *Communications Materials* 2.1 (2021), p. 30. DOI: 10.1038/s43246-021-00134-1.

[45] Linn Leppert, Tonatiuh Rangel, and Jeffrey B. Neaton. “Towards predictive band gaps for halide perovskites: Lessons from one-shot and eigenvalue self-consistent GW”. In: *Physical Review Materials* 3 (2019), p. 103803. DOI: 10.1103/PhysRevMaterials.3.103803.

[46] Falco Hüser, Thomas Olsen, and Kristian S. Thygesen. “How dielectric screening in two-dimensional crystals affects the convergence of excited-state calculations: Monolayer MoS_2”. In: *Phys. Rev. B* 88 (24 Dec. 2013), p. 245309. DOI: 10.1103/PhysRevB.88.245309. URL: https://link.aps.org/doi/10.1103/PhysRevB.88.245309.

6 Acknowledgements

First of all, I am deeply grateful to Professor Claudia Draxl for giving me the opportunity to work on this project. I also thank Dr. Cecilia Vona and Sven Lubeck for their detailed and kind guidance from the very beginning. Also I am thankful to Benedikt Maurer and Ignacio Gonzalez for helping me understand and carry out the BSE calculations, and to Hannah Kleine for providing clear guidelines on local orbitals. I also thank everyone in the sol group.

I owe profound thanks to my parents for their trust and financial support. I also dedicate special thanks to my Angela grandma in heaven, who always supported and believed in me. Finally, I extend my heartfelt thanks to my family and friends for their constant encouragement and support.